

SATELLITES-SPACECRAFT MATERIALS AND HYPERVELOCITY IMPACT (HVI) TESTING: NUMERICAL SIMULATIONS

Iliescu, L. E., Lakis, A. A. & Oulmane, A.

Mechanical Engineering Department, École Polytechnique of Montréal, Canada
C.P. 6079, Succursale Centre-ville, Montréal, Québec, Canada H3C 3A7

ABSTRACT: *Damage due to hypervelocity impact (HVI) of micrometeoroid and space debris (MMOD) is a common threat in the current space environment for any spacecraft orbiting the Earth and for future launches of new spacecraft. For this reason, the choice of structure and protection materials is an important issue during the design and manufacture of spacecraft. These materials must be chosen based on their survivability in the space environment. The probability of an HVI of MMOD is determined based on a specific impact risk assessment procedure. Starting from identification of the most commonly-used materials for the manufacture of spacecraft and sorting them into three main groups; metal alloys, composites and sandwich panels, the present work presents the results of time-frequency analysis of the signals obtained from numerical simulations of HVI. The damage detection method is based on applying a Choi-Williams Distribution (CWD) and a specific TF-Analysis algorithm developed in-house. A student version of LS-Dyna software was used to carry out these numerical simulations. For the case of penetration, the CWD method reveals clear differences in the HVI form and frequency amplitude for one or two materials of each group initially identified. The characteristics of each perforation on the materials investigated are discussed and results obtained are corroborated through analysis of the signals collected during a previous HVI test session.*

KEYWORDS: Satellites-spacecraft materials, hypervelocity impact (HVI) testing, numerical simulations

INTRODUCTION

W. P. Schonberg (1) presents an overview of the results of impact tests performed on spacecraft structures made with various materials; metallic (mostly aluminium) and composites or honeycomb sandwich panels (HC/SP). The paper focuses on HVI tests on composite materials, where the impacted materials behave as fluids and the impact creates extensive internal damage (e.g. delamination), and on metallic targets when the damage extends further than the crater/hole diameter. Advantages of composites in the case of an HVI are presented, including less ejecta or the decrease in total weight compared with metals. Regarding the use of composites for MMOD protection, dual-wall outer bumper systems (2) made from Kevlar and graphite /epoxy (Gr/Ep) were considered, however they do not offer any advantages compared with an Al dual-wall system. Other solutions that

performed marginally better were CFRP/metal matrix, ceramic materials or porous fillers combined with Al bumpers.

As inner bumpers, Kevlar and Spectra panels were tested and results demonstrate that the use of composite offers increased protection to hypervelocity impacts (3). A paper by Frank Schafer (4) investigates use of new materials in different configurations to increase spacecraft protection to HVI. The paper also discusses advantages that can be gained by incorporating light layers of materials such as thermal blankets or multi-layer insulation (MLI), depending of their position in the configuration. Tested configurations were: bi-layered aluminium foam bumpers (AlSi7Mg at 10, 20 and 30 ppi- pore per inch) with a density from 7% to 10%, flexible stuffing made from Nextel 312AF62 or Kevlar alone or in combination with polyurethane foam layers, titanium alloys (Ti6Al4V) or different hybrid configurations mixing these type of bumpers. The paper concludes that the aluminum foam is capable of inducing multiple shocks to the projectile, the Ti and Al alloys show superior capabilities in inducing shock to the projectile and that flexible stuffing is capable of absorbing the energy of a debris cloud.

Frequently used materials in the manufacture of the spacecraft

Aluminium

Aluminium alloys have been tested in different configurations. For example, in a recent paper by Wan H (5) the performance of 2024 aluminum alloy panels stacked together with CFRP panels was studied to determine whether this configuration improves the resistance of a laminate panel shield. Results showed a significant reduction in the HVI peak shock pressure. Increasing the layer number further increases shielding performance.

G. S Guan (6) studied the HVI test capability of an Al bumper coated with ceramic. Results showed more effective shattering of projectiles impacting the coated side of the panel, into smaller particles with lower kinetic energy. Gong WW (7) presents the performance of aluminium foam in absorbing HVI energy using a three- dimensional material point model (MPM3D). Results compare well with experimental data. Smoothed Particle Hydrodynamics numerical simulations on aluminum foams with homogeneous open-porosity, cell sizes about 1.6 mm and relative densities near 26.9% were conducted by Ma ZT (8) with similar results showing the effectiveness of Al foam in absorbing HVI energy.

Honeycomb panels

Honeycomb sandwich panels (HC/SP) are frequently used in primary satellite structures. The effect of HVI on these panels has been studied by many authors. In a recent paper, Ping Liu (9) simulated HVI on sandwich panels and determined the influence of internal structure parameters on the results of typical impact conditions such as oblique impact, previously studied before by Taylor (10, 11). The results showed that the impact angle has only a marginal influence on the perforation limit. The study uses a material point method (MPM) – based internal structure model to describe the response of HC/SP to HVI. The MPM uses a set of Lagrangian points and an Eulerian background grid. The Lagrangian

points carry all the physical variables (mass, velocity, stress and strain) and show the deformation of the material and imply the boundary of the domain. The Eulerian background grid allows solution of momentum equations and calculates spatial derivatives. At each step, the Lagrangian points are bound to the Eulerian grid and they deform together. In order to validate the model, the results were compared with the ballistic limits obtained during previous tests performed by Turner (12) on HC/SP with Al2024-T81 facesheet material and a Al5052-H19 honeycomb core. A thin layer of 0.1 mm Teflon was added to the front facesheet. The study concludes that the hole diameter of the front facesheet is influenced much more by the projectile's size than its speed. In comparison, the hole diameter on the rear facesheet is influenced by both the impact velocity and the projectile size. The following parameter changes decrease the channelling effect: increasing cell size, reducing the thickness of the cell wall or reducing the thickness of the entire honeycomb core.

J.-M. Sibeaud (13) presents HVI test and simulations results done on structural bodies that represent those used in satellites. The HC/SP used were 150x150 mm or 150x190 mm and consisted of 20 mm aluminum honeycomb cores (0.025 mm thick aluminum sheets) glued together with 0.8 mm aluminum face-sheets. Five HVI tests were performed at 5.7 Km/s with a 7 mm diameter projectile. The paper describes the honeycomb channelling effect: the projectile and front facesheet fragments are absorbed within the honeycomb structure and concentrate on the rear face-sheet, creating holes with diameters more than 10 times that of the projectiles. HVI simulations done with the Ouranos hydrodynamic software (13), showed the same results, *Figure 1*.

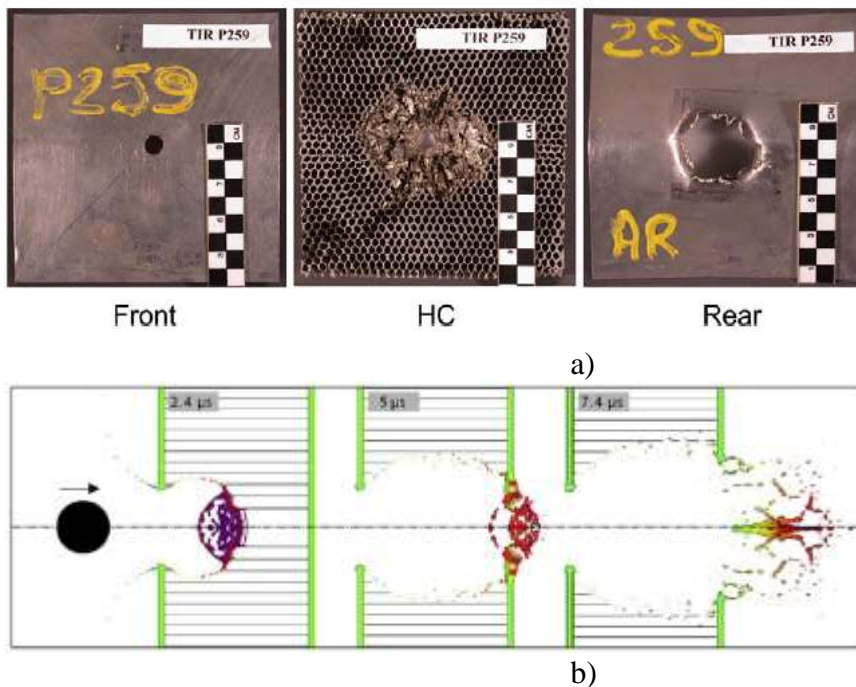


Figure 1: Channelling effect created in an HC/SP impacted at 5.7 Km/s; a) test samples, b) simulation (13)

S Ryan (14) studied the HVI test performance of metallic open-cell foams to evaluate whether this material could replace honeycomb sandwich panels (i.e. eliminate the channelling effect in the honeycomb core). They hoped they could obtain better protection results with the same mechanical and thermal performance and at the same weight. For his experiments the author used a baseline target containing two honeycomb sandwich panels spaced at 2 cm with two outer layers of stainless steel mesh. Results of this configuration were compared with those obtained on 12.7 mm thick open-cell Al6101-T6 foam panels (pore density; 10 pores per inch - ppi). After 19 HVI tests the authors conclude that the metallic foam configuration performs better in fragmenting and melting the projectile, and therefore the impact energy on the rear walls are reduced. However, oblique HVI test results showed a decrease in configuration shielding performance which was attenuated by the presence of outer layers of metallic mesh.

Ceramic foams are used in HVI tests due to their unique combination of properties such as low density and high stiffness, which provides very good shock absorption, Silicon oxycarbide (SiOC) microcellular foams can be used to enhance the effectiveness of sandwich panels (15).

Recently, a Smoothed particle hydrodynamics (SPH) method was used by Pilseong Kang (16) to model the HVI on HC/SP and determine the most influential parameter on the channeling effect. The material used for the facesheets was Al 7075-T6 at 0.4 mm thickness, the HC core was Al5056 with an average of 30 mm core depth, cell size and thickness were 4.8 and 0.025 mm respectively. The projectile material is an aluminum alloy with a density of 2.78 g/cm³. Different diameters were launched at high speeds up to 7.2 km/s. Simulation results agreed with experimental tests and showed that the HC core cell size is the most influential parameter on the damage of the rear facesheet due to the channeling effect. The critical projectile diameter decreases due to the presence of HC core and varies with the HC core cell size.

A complete study of HVI on HC/SP is presented by W. Schonberg, (17). 400 HVI tests results are analyzed, leading to the development of a system of empirical equations that can be used to predict the trajectories and spread of debris clouds that exit the rear facesheet. These equations are a good fit to the data and are capable of taking into account most of the variations in test conditions with a correlation coefficient ranging from 60 to 90%. The study predicts the minor and major hole dimensions for the HC/SP facesheets and the trajectory and spread angles for normal and in-line dust & debris clouds for HC/SP with aluminium and composite face-sheets. Based on this development, we can determine what spacecraft components will be impacted by the mass of debris cloud and to what extent. This information can be introduced into a risk assessment algorithm to calculate the probability of spacecraft failure under a prescribed set of impact conditions.

An improved HC/SP configuration for satellite structures (Al and Ca honeycomb or Composite and Al honeycomb) is presented by R. J. Turner (12). Among the alternate configurations presented: MLI + a front/intermediate material layer or multiple honeycomb layers; the material layer could be Nextel, Kevlar or Al mesh. Two types of MLI are

studied; enhanced and toughened MLI. The enhanced MLI (EMLI) is used with four layers of betacloth and nine layers of Kevlar 310. The toughened MLI (TMLI) is used with three layers of betacloth. Alternate honeycomb designs include; a double honeycomb (DHC), a single HC with an intermediate 0.4 mm facesheet bonded to the core, and a reinforced honeycomb (RSHC). The single HC has an additional 0.2 mm Al bonded to the facesheets. A series of HVI tests were performed at velocities up to 8 km/s. New ballistics limits were quantified and tests showed that at 5 km/s the critical diameter of the projectile increased from 1 mm to 1.8 mm for the DHC with TMLI and to 1.93 mm for the SHC and EMLI. Turner observed that use of a DHC instead of a SHC reduced the number of penetrations by a factor of 3.7 and use of a MLI reduced the penetration 4.6 times.

Warren J. (18) presents the results of HVI tests performed on foam core sandwich composite specimens infused with a shear thickening fluid (STF). Two 0.064 cm thick aluminum facesheet sandwich composites (1.27 cm thick open cell, 2 pores per cm aluminum foam cores) were filled with an STF consisting of 0.2 mass fraction Aerosil 200 fumed silica in 200 molecular weight polyethylene glycol (PEG). Two more identical foam core specimens were filled with only PEG. The HVI tests were performed at velocities of 3.8 Km/s using a stainless steel projectile of 1 mm diameter. Results showed that most of the impact energy was dissipated within the proposed sandwich composites, with almost no damage on the rear wall.

In a recent conference paper presenting the Lunar Atmosphere and Dust Environment Explorer (LADEE) project, Eldon P. (19) suggests a “low-cost, reusable, spacecraft bus architecture for future Planetary Science missions”. LADEE’s uses co-cured structures based on sandwich construction (HC/SP). The skin materials (SP) include carbon fiber and epoxy matrix (resin) glued to the honeycomb core with a film adhesive and the radiator panel skins are aluminum.

Composites

Another configuration that offers enhanced resistance to HVI for satellite structures (e.g. Radarsat-2) is composed of CFRP facesheets bonded to Al honeycomb cores, S. Ryan (20). A series of 55 HVI tests were performed using a 2017-T4 Al projectile of 1.25 mm diameter. The different configurations studied are presented in *Table 1*.

| Panel | AD (g/cm ²) | Facesheets | | | Honeycomb | |
|-------|-------------------------|------------|--|---|------------------|--------|
| | | t (mm) | Material | Stacking | Configuration | t (mm) |
| RAD1 | 0.7017 | 1.45 | FL01 (F)-HMF196/34 T300-1k fabric/ FL02 (P)-HYE 4934C K139 u.d. ply | (0 _F /0 _P /+45 _P /90 _P /-45 _P /-45 _P /90 _P /+45 _P /0 _P) | 3/16-5056-.001P | 50.6 |
| RAD2 | 0.5847 | 1.40 | FL01(F)-HMF196/34 T300-1k fabric/ FL02(P)-HYE 4934C K139 u.d. ply | (+45 _P /0 _P /-45 _P /+45 _P /90 _P) _S | 3/16-5056-.001P | 25.3 |
| RAD3 | 0.4217 | 1.15 | FL01(F)-HMF196/34 T300-1k fabric/ FL02(P)-HYE 4934C K139 u.d. ply | (0 _F /0 _F /+9 _P /-9 _P /+9 _P /-9 _P /+9 _P /-9 _P /0 _F /0 _F) | 3/16-5056-.001P | 12.1 |
| GOCE | 0.7807 | 2.30 | M18/32%/M55J/145 u.d. ply | (+45/0 ₂ /-45/0 ₂ /+45/0 ₂ /-45/0 ₂ /+45/0 ₂ /-45) | 3/16-5056-.001P | 12.5 |
| SAX | 0.4405 | 0.95 | 914/34%/137/6K/M40B u.d. ply | (0/+60/-60) _S | 3/16-5056-.001P | 29.7 |
| H/P | 0.2300 | 0.55 | M18/G801 u.d. ply | (+45/0/90/-45) | 3/16-5056-.0007P | 19.9 |

Table 1: Different satellite CFRP- Al honeycomb structures HVI tested (20)

The results of the tests were also used to determine the ballistic limit equations for these types of configurations.

In an early paper, Timothy C Thompson (21) presents the development of spacecraft structures made entirely of composite materials as an alternative to an all-aluminum spacecraft bus. His analysis is based on fundamental principles: simplicity, modularity and interchangeability. The use of graphite/epoxy produced a weight saving of 46 pounds including additional solar array substrate (SAS) panels, 0.020" thick (pre-cured panel assemblies of Gr/ET -50/ERL 1962. [0/45/90/135] with either co-cured 0.2 mil copper on one side or co-cured 2.0 mil Kapton) weighing 33.9 pounds. The satellite decks are manufactured similarly to the SAS panels (except copper was co-cured on both sides of the deck) and the middle and the lower decks have a one inch thick aluminum core. The space frame is made from flat laminates. The skin thickness on all decks is 0.030" with an orientation of [0/60/120]s and the frame subassemblies are made from flat 0.048" thick laminates of T50/ERL 1962 with a [0/45/90/135]s orientation.

Non-metallic spacecraft structures, CFRP, are also mentioned by M. Nicoletto (22) as a potential replacement for standard aluminium panels. This alternative eliminates occurrence of electromagnetic interference with high speed digital lines used for data distribution. The CFRP consists of layers of laminates in which several plies are rotated (for mechanical strength). The plies are made of carbon fiber (25 fibers at 10 μm diameter) impregnated in an epoxy resin matrix. The epoxy/carbon fiber composite is generally composed of 57% (by volume) carbon fiber with inter-laminate epoxy layers (M21) to electrically insulate each consecutive carbon fiber layer. The thickness of each carbon fiber layer is about 200 μm while the M21 interlayers are approximately 35 μm thick.

In a recent paper, Changqing and Bo (23) analyze three different configurations and present the improved performance of a laminate of aluminum/CFRP layers compared to a single aluminum layer or a single CFRP layer of the same areal density. The multilayer shield made the projectile rebound multiple times and, at high intensities, the projectile was more fragmented. This result clearly proves that the designed multilayer shield is more effective against HVI.

One paper presented at the 55th AIAA conference (24) compares the results obtained on two different composite laminates. The laminates were made using epoxy-reinforced, pre-impregnated, unidirectional carbon fiber; a quasi 3D five-harness satin weave (Q3DO5) and a cross-ply with and without a graphite sheet bonded on the impacted side. The HVI impact tests were performed at velocities of 2.9 to 5.25 Km/s and the results suggest that the targets equipped with a graphite sheet had increased tolerance to HVI.

Modelling of HVI damage in composite is discussed in a multitude of papers. One recent study by Aleksandr Cherniaev (25) presents an explicit mesa-scale representation of two numerical tests on thermoplastic AS4/PEEK (APC-2) materials with quasi-isotropic layups. To more accurately reproduce the fracture mechanism that occurs in an HVI, the composite laminate used for the simulations is represented as a structure composed of alternating fiber-reinforced and finite-thickness resin-rich layers. The material model was characterized in terms of stress-strain relations, equations of state (EOS), failure initiation criteria and post-failure response. The simulation employed a combination of SPH and the

finite element method (FEM) in a Lagrangian formulation to represent the aluminum projectile and the laminate composite. Results showed a good correlation with experimental data in terms of delamination area and external damage. They also showed that the dynamic fracture toughness is an essential element that must be considered to allow higher accuracy of simulation results.

Q. Gua (26) investigates HVI damage in 55% TiB₂/2024Al composite intended to replace 6061 and 2024 aluminum alloys that are currently used on spacecraft structures. For this study 2024Al alloy spherical projectiles with diameters of 1.2 and 1.5 mm were launched from a two-stage light gas gun to reach an impact velocity of 2.5 km/s. According to the results, the TiB₂-Al interface formed a new Al_xO_{1-x} phase and a crystal parameter of 0.69 nm. The TiB₂ particle formed a stacking fault with a width ranging from 10 to 20 nm. The formation of nanograins (about 100 nm) was noticed within the Al matrix due to dynamic recrystallization and the lamellar S' phase was transformed into a lenticular or spherical S phase after HVI.

A. H Baluch (27) studied the HVI on a satellite carbon-epoxy composite wall with a stacking sequence of [(0/±45/90)₂]_s. The satellite wall, with 16 layers of carbon-epoxy composite that had been previously exposed to the characteristics of an LEO environment, was impacted at an oblique angle by an Al2017 projectile of 5.56 mm diameter. The results were compared with data for normal impacts, for both Aluminium alloys and composites, and showed that oblique angle impacts lead to multi-axial loading on the composite wall, resulting in more complex behavior than the normal angle case. Also, the energy absorbed by the non-aged composite laminate is on average 20 Joules more, which shows that the oblique angle impact energy absorption is larger in comparison with normal impact on composites or on 6061-T6 aluminium alloy plate. This energy absorption will increase with an increase in velocity. In terms of percentage, 35% more energy is absorbed at an oblique angle of 45°. The energy absorption of the composite wall with oblique angle HVI was almost 1.85% higher than that of the Aluminium alloy.

Cheng Wing L (28) presents a new impact model for thick composites based on HVI tests at velocities up to 2 km/s. For the first testing session at 0.6 m/s various woven polymeric composites containing S-2 glass fibers and polyester resins were used. The thickness of the laminates was 4.45 cm. The second series of tests were performed at 1.83 m/s and materials tested were Kevlar reinforced plastics, S-2 glass reinforced polyester, rolled homogenous steel, 7039 Aluminum, high hardness laminates, and ceramic (Al₂O₃) laminate or chemically bonded ceramics.

B. Aissa (29) presents a new concept of embedding a self-healing process within a CFRP laminate using microcapsules filled with 5E2N monomer combined with spread catalyst particles (Ruthenium Grubbs). HVI tests were performed using projectiles of 4 mm diameter launched at velocities between 1.3 and 1.7 km/s. Although the microcapsules would not heal the perforation hole itself, healing of potential delamination that developed around the crater/hole was evident.

Oleg V. Startsev (30) investigates hybrid composites composed of carbon and glass fiber reinforced plastics (CFRP, GFRP) assembled using epoxy with several alternative surface protection materials: AZ alloy AMG-Gm, aluminum foil. Lacquer and paint coating LKF 40-1-1 14-87. These materials were used on Salyut-type spacecraft that have spent long periods of time in outer space.

Lei Wang (31) studied T300/ epoxy-resin high-performance composite material, which has been widely used in aircraft, spacecraft, watercraft and transportation because of its excellent mechanical characteristics. The authors developed an approach to predict fatigue life based on a fatigue damage accumulation model built on stiffness degradation, according to damage mechanical theory.

Hoffman (32) describes the use of high-performance composite materials (K1100 graphite fiber/cyanate ester matrix [Gr/CE]) for the structural design of a small satellite. In addition to discussing requirements for structural performance, detailed design, procurement and testing, the paper also presents a thorough material selection analysis.

Bulk metallic glass (BMG)

Starting from ballistic limit equations, Lee Hamill (33) investigates a new type of material that should have high hardness at the lowest possible density. The low melting temperature is an additional advantage since it allows faster vaporization of fragments and provides increased toughness in order to carry the launch loads. Based on these properties the author proposes a bulk metallic glass (BMG, amorphous metal) thicker than 1 mm, with densities similar to other crystalline alloys (e.g., titanium) but with hardness typically found in ceramic materials. BMGs can have much higher toughness than ceramics. The study presents a series of HVI tests on BMG Vitreloy 1 ($Zr_{41.2}Ti_{13.8}Cu_{12.5}Ni_{10}Be_{22.5}$) and the BMG matrix composite DH1 ($Zr_{36.6}Ti_{31.4}Nb_{7}Cu_{5.9}Be_{19.1}$) at velocities ranging from 0.8 to 2.79 km/s using an aluminum spherical projectile 3.17 mm in diameter. Results showed that Vit 1, DH1 and DH3 samples exhibit increased impact resistance and motivates the use of amorphous materials in spacecraft structures.

Davidson M and all (34) also investigated the HVI protection qualities of amorphous metal composites which are usually multi-component alloys containing titanium, zirconium, copper, aluminum, niobium or beryllium. Samples thicker than 1 mm are vitrified and become BMG. Different thin panel BMGs and multi-faced egg boxes were HVI tested at velocities up to 5.5 km/s. The study demonstrates that welded panels of BMG composites offer a unique HVI protection solution for future satellites.

Douglas C. Hofmann (35) integrated layers of metallic glasses in order to improve the HVI protective capability of a Whipple shield. The recent study showed that a debris cloud could be significantly diffused by corrugating the bumper shield's surface. Also, the cellular structures created by welding corrugated panels together could prevent penetration of the projectile. The metallic glass used in the study is a commercially available ribbon of Metglas 2605 SA1 with a Vickers hardness of 900, compared to 107 for Al-6061. On the other hand, the density of the Metglas is 2.7 times larger than Al-6061. To make the internal

stuffing for the Whipple shield, 21 cm square sheets of the metallic glass ribbon were cut and then stacked together, maintaining the same areal density as the actual spacecraft baseline. The configuration was impacted at an average velocity of 7 m/s using a 2.8mm diameter Al-2014 T4 sphere. The configuration that includes the metallic glass showed improved performance. The paper also mentions some new materials; metallic glass alloys that have a lower density than the alloys that have been used in current (and previous) studies, low-density metallic glasses developed in Al-based systems (2.8–3.6 g/cm³), Mg-based systems (2.6–4.2 g/cm³), Ca-based systems (1.9–2.6 g/cm³), and Ti based systems (4.5–7.2 g/cm³).

Fabrics: Nextel, Spectra and Kevlar

S Katz (36) studied the response of micro-composites exposed to HVI. In this research the materials are Kevlar 29/epoxy and Spectra1000/epoxy thin film micro-composites (thickness of about 100 μm). These materials are used extensively in spacecraft structures and satellite components such as antenna struts, panels and low distortion frames (high specific strength, high stiffness and low coefficient of thermal expansion). The targets used are films made using epoxy resins (Araldite LY564, Ciba-Geigy mixed with hardener HY560). The different type of fibers used were; UHMWPE fibers (Ultrahigh molecular weight polyethylene, Spectra 1000 fibers), surface-treated Spectra 1000 fibers (referred to as Spectra-RF), and Kevlar 29 poly (paraphenylene terephthalamide), *Table 2*.

| Property | Spectra | | | Explanation |
|-----------------------|-----------------------|-------|------------|---|
| | Kevlar 29 | 1000 | Spectra-RF | |
| σ_f (GPa) | 3.1 | 3.9 | 1.5 | Fiber ultimate strength |
| E_f (GPa) | 65 | 175 | 175 | Fiber Young's modulus |
| N | 4 | None | 5 | Number of broken fibers |
| n | 7 | 7 | 7 | Number of embedded fibers |
| r (μm) | 6 | 13.5 | 13.5 | Fiber radius |
| ϕ_f | 2.64×10^{-3} | 0.013 | 0.013 | Fiber volume fraction $\phi_f = n\pi r^2/tw$ |
| τ (MPa) | 24.6 | 5.8 | 11.8 | Interfacial shear strength |
| t (μm) | 100 | 100 | 100 | Specimen thickness |
| L_{dbr} (mm) | 1.4 | 2 | 2.5 | Fiber debonding length |
| w (mm) | 3 | 3 | 3 | Specimen width |

Table 2: Material properties of micro-composite targets (36)

The targets were impacted with a 1 mm diameter aluminium flyer at velocities up to 3 km/s using a laser driven flyer plate (LDFP) system. The micro-mechanical response of different

micro-composite materials to HVI was studied before the tests and HVI damage characterization of 50 specimens showed permanent damage such as the crater holes, fiber breakage, fiber pull out and fiber de-bonding. Conclusions were based on the main fracture mechanism of each micro-composite (absorbed energy calculated for the classical absorption mechanisms). For the Kevlar 29 based composites both the matrix and fiber were damaged due to the strong interfacial strength; the dominant fracture mechanism was fiber pull out. In the case of Spectra 1000/epoxy, new surface creation was the main damage mechanism. For Spectra-RF, prior etching in oxygen RF caused fiber surface restructuring and increased the interface strength, leading to cracks in the matrix and breakage of the fiber as well as fiber pull out. The untreated fiber failed predominantly by fiber/matrix separation.

Nextel and Kevlar cloth materials (fabric or a flexible woven material consisting of a network of natural or artificial fibres often referred to as thread or yarn) are especially used in internal bumpers for different shield configurations. They have been studied by many authors in relation to HVI and their conclusions mainly confirm the same capabilities: Nextel is able to shatter the projectile and dissipate the impact energy whereas Kevlar is useful for catching the projectile fragments and absorbing their impact energy.

Eric P. Fahrenthold (37) presents the results of HVI simulation on a shielding configuration that used Kevlar aramid fiber 129 and Nextel woven cloths. Results are compared with test results presented in a prior report by Grosch (38). The simulations were done for two types of projectiles one of inhibited shape charge (ISC) a hollow cylinder and the other of spherical shape at a velocity of 11 km/s. The simulations required 252 hours and the output underestimates actual composite shield performance. HVI simulations characteristically carry high computational cost.

Fused silica/windows materials

HVI on spacecraft windows used for navigation or observation, especially fused silica (SiO₂) windows was studied by R.R. Burt and E. L. Christiansen (39) for a wide range of projectile types. The target is a high purity synthetic amorphous silicon-dioxide, 76 mm diameter. The principal projectile is a 0.4 mm diameter Al2017-t4 sphere (other projectile materials used were steel, nylon, aluminum-oxide and copper alloy). Projectile velocities up to 7 km/s were tested at different impact angles. Other HVI tests were carried out on Chemcor windows which are made of two panels of chemically tempered silica with a laminate silicon interlayer and on Hyzod -AR polycarbonate, a transparent amorphous thermoplastic with a hard coated surface. The paper concludes that Hyzod polycarbonate has an improved penetration performance compared to Fused Silica at the same mass per unit area and the Chemcor glass showed the least HVI performance compared with the other two materials.

A paper, written by Song LiHong (40), analyzes the HVI on fused silica, an appropriate optical material used on spacecraft for sensitive surfaces such as mirrors or sensors. The experiment uses the same LDF launcher to shoot an aluminium flyer of 16 μ m thickness at

velocities up to 3.7 Km/s onto a transparent glass (fused silica glass) target of 15 mm thickness and 40 mm diameter coated with a metal or non-metal film. The HVI damage morphology was measured with an optical microscope and a scanning electron microscope (SEM). Damage types observed included cratering, ejecta and micro-cracking. These damage types are caused by the non-homogeneity of surface and optical absorption or scattering and depend on the optical constant of the fused silica and the surface morphology of the target.

Other materials solutions

X. Huang (41) proposes a new material, an amorphous alloy that could be used to improve the performance of a Whipple shield. It consists of a Fe-based amorphous alloy coating and an LY12 aluminum alloy substrate and is used as the first bumper of the shield configuration. The coating materials are amorphous Fe–Si–B ribbons of 50 μm thickness, with a nominal composition of Fe₇₇Si₁₄B₉. A 2.85 mm thick LY12 aluminum alloy substrate is used. Four tests were performed at impact velocities 3.5 and 5.5 km/s launching 4 mm spherical projectiles of solid LY12 aluminum alloy. Results showed that this type of configuration performed better at the lower speed. At 5.5 km/s the shield still performed slightly better than the baseline, leading the authors to conclude that an amorphous alloy reinforced bumper can create higher shock pressures and induce a higher temperature rise in the projectile.

Materion Beryllium & Composites (42) provides materials such as Beryllium for satellites, with the lower cost version Al Beryllium for structures and optics, or Supremex as a replacement for Titanium. These materials offer qualities that are favourable for use in a space environment including; light weight (less than aluminum), high specific stiffness and thermal stability, good thermal conductivity, high melting temperature or heat capacity and dimensional stability.

Serhan Avcu (43) discusses the process of structural material selection for spacecraft focusing particularly on the atomic oxygen (AO) effect (LEO environment) but also considering space environmental effects. Structural materials for this application must have properties including light weight, high stiffness and dimensional stability and therefore commonly-used metals are Aluminum, Magnesium Beryllium, Titanium, Molybdenum, Tantalum and Tungsten. Polymers are used for the central body structure of communications satellites and antenna reflectors, temperature resistant parts, electronics, communication and power devices, life support systems, sensors and detector structures. The most popular of these materials are Kapton, Teflon FEP, Polysulfone, Mylar, Tedlar, PEEK, Halar and Kevlar. In terms of protective coatings (AO), polycrystalline ceramic films such as SiO_x (1.9<x<2.0), SiO₂, fluoropolymerfilled SiO₂, Al₂O₃ and Germanium have proven to be effective in protecting polyimide Kapton.

Although they are not used for satellite structures, Kapton films (44), which are often used for thermal control blankets were also HVI tested using a laser driven flyer (LDF) system at velocities up to 2.9 km/s. The damage created was analyzed for low and high velocities

(starting at 1.7 km/s). The Kapton HN polyimide films used as targets had three different thicknesses; 25, 50 and 125 μm in order to reveal the transition from brittle to ductile fracture as the thickness increases. This fact is explained by the capacity of Kapton film to absorb more energy and reduce its strain rate as it becomes thicker. Moreover, as the projectile velocity increases the fracture morphology changes, presenting a different fracture mechanism that can be explained by the high temperature gradient created when the flyer hits the polymer target. The paper concludes that brittle fractures occur at low velocities, and these fractures become ductile as the thicknesses increases. At high velocities ductile fractures are observed in the central region of impact and brittle fractures occur in remote areas of the target.

The effect of HVI on polymers is also presented by R. Verker (45) using the same experiments; a laser drive flyer (LDF) launches projectiles of dimensions ranging from 10 to 100 μm at velocities up to 3 Km/s.

Irina Gozaman (46) presents an effective protective solution for coating of Kapton polyamide which is widely used for the external surfaces of spacecraft in low Earth orbit (LEO) exposed to atomic oxygen (AO) and to problems of electrostatic discharge (ESD). The coating, 100-300 nm thick, is deposited on Kapton at near-ambient conditions by LPD using an aqueous solution of a metal-fluoride complex and boric acid. The protective performance of the oxide-coated Kapton is analyzed using methods such as atomic force microscopy (AFM), electrostatic force microscopy (EFM), scanning electron microscopy (SEM), Rutherford backscattering (RBS) and X-ray photoelectron spectroscopy (XPS).

A.A. Voevodin (47) presents a tribological coating concept intended to improve the reliability of satellite systems degraded by the characteristic conditions of the space environment; atomic oxygen, solar radiation, energetic particles, and temperature cycling. The coating is applied in order to change the surface chemistry and adapt the structure to the environment. The first coatings were made of WC, WS₂, and the diamond-like carbon (DLC). The second series of coatings tested were made of yttria stabilized zirconia (YSZ) in gold or in an Al₂O₃ matrix, with encapsulated nano-sized reservoirs of MoS₂ and DLC. The toughness was enhanced using a grain boundary sliding mechanism.

Joo Hyun Han (48) studied multi-walled carbon nanotube (MWNT)/epoxy composites that were fabricated at different nanotube concentrations (wt %) and exposed to the LEO space environment. The MWNTs (>95% purity) were used as filler and synthesized by CVD, thermal decomposition of hydrocarbon. The diameter and the length of the MWNT were 10~20 nm and 10~50 μm respectively. The epoxy (from HK fiber Co.) used was a copolymer solution composed of acetone, anhydride-type resin and hardener.

Improved protection of satellite structures from the effects of space debris impacts by using a glassy-rubbery layered block-copolymer nanostructure is presented by Jae-Hwang Lee (49). The paper presents a microscopic ballistic test using a micron-size silica sphere as the projectile, shot by an energetic laser pulse. Different responses were observed, depending on the orientation of the layers in the nano-composite. However, the compression-dominant response for impacts that are perpendicular to the layer orientation dissipates the impact

energy more efficiently than impacts that are parallel to the orientation. A 30% reduction in penetration depth was made possible by proper orientation of the layers.

Materials review summary

Our materials review concludes that there is a variety of materials that could be used for satellites structures and most of these materials have already been HVI tested.

Depending of the goal that is pursued, design or operational considerations, these materials can be grouped in three large categories:

- Metal alloys such as aluminum, steel, titanium alloys or newer alloys such as beryllium
- Composite materials, different types of fibers (glass, carbon or aramid fibers) usually imbedded in a matrix (epoxy, ceramic or metallic)
- Honeycomb sandwich panels with different types of facesheet materials (from different types of alloys to composites) and different cores (honeycomb to ceramic or metallic foam)

A comprehensive review of the materials properties of these different groups has been presented by Francois Cardarely (50) whereas information on satellite material selection is presented by J. Wijker book (51) or C. Annarella (52).

For our HVI study, LS- DYNA software is used to simulate impacts on one or two materials from each of the identified groups. The simulation targets are square (12cmx 12cm) and the same projectile is used for all simulations; a sphere of Al 2017 T4, 0.3125 mm in diameter.

The attached *ANNEX* presents tables of the most-used satellite materials. Materials from each of the above-mentioned groups are chosen from these tables for our HVI test simulations.

HVI test simulations

Introduction

Three main approaches are used to investigate the damage on a spacecraft caused by hypervelocity impact of orbital debris:

- Physical testing, which is generally expensive and limited by current technology. Existing projectile launchers are not capable of covering the entire range of observed impact velocities, dimensions and form of actual space debris particles. On the other hand, tests can be done at velocities up to 8-9 km/s, which mimic a significant portion of real space debris impacts.
- Analytical methods, such as ballistic limit equations developed by Cour-Palais [53], shield sizing equations developed by Christiansen [54] and Reimerdes [55], and impact damage equations developed by Watts [56]. Assumptions are generally applied to simplify these equations for a limited range of situations without compromising their validity.
- Numerical/simulation methods derived from experimental data. This approach can be used for a variety of cases, and offers special insight for velocities that are out of the testing range. The accuracy of HVI simulation results are influenced by the degree of

details used, by the material models and equations of state. Conventional numerical methods; Eulerian, Lagrangian and Smoothed Particle Hydrodynamics (SPH) or hydrocodes are generally ill suited to address important features of MMOD impact. New methods proposed in recent literature use a parallel hybrid particle –element model. These particles help model inertia, contact impact, thermodynamic and compressed states and element modeling of strength effects, tension and elastic-plastic shear. Some of the models that use Lagrangian methods were used by Beneneti [57], Guangyu [58] or Bashurov [59] in order to simulate impact damage more accurately.

The latter two of the above three approaches must be validated by comparison with physical test results.

Two alternate finite element modeling methods are used to describe the motion of material in space; a Lagrangian (body fitted coordinates) or Eulerian (fixed in space) grid, and meshless methods (Lagrangian without grid), also called SPH, *Figure 2*.

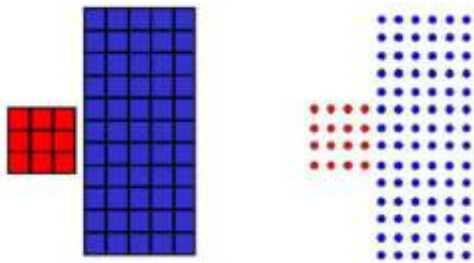


Figure 2: Grid based modeling and meshless discretization of an HVI [60]

The following *Table 3* presents a comparison between the three modeling methods using modeling criteria specific to HVI.

| Characteristics/models | Lagrangian | Euler | SPH |
|--|----------------------------------|-------|-----|
| History dependent | Yes | No | Yes |
| Representing high material deformation | No (rezoning, erosion technique) | Yes | Yes |
| Simulating diffusion and mixing problems | No | Yes | Yes |
| Accuracy of debris cloud | No | No | Yes |
| Instability(lack of nodal completeness) | No | No | Yes |

Table 3: Lagrangian, Euler and SPH method comparison table

SPH modeling is the most promising method in simulating HVI impact. For our simulation however, we utilise a finite discrete element Lagrangian method similar to the one used by R. Vignjevic [61]. This choice is made due to various facts, such as; the impact velocities used (in order to compare with physical tests previously performed) are in the low velocity regime, resources are limited (time and computational), and criteria related to accuracy are not a priority. All of our simulations were performed using a LS-Dyna student version [62].

Impact numerical formulation

For our simulations we started by applying a common method used in solving an engineering problem; discretization of the impact components using a grid of nodes connected together, and modelling the target and projectile using connected grid nodes. Upon impact the connections are broken, the impact effects propagate but the element remains intact in order to conserve its mass and momentum.

The Lagrangian finite element grid based method employed here is mainly used in structural dynamics and has the following conservation equations:

LAGRANGE

Mass:

$$\dot{\rho} + \rho \frac{\partial u_i}{\partial x_i} = 0$$

Momentum:

$$\dot{u}_i = f_i + \frac{1}{\rho} \frac{\partial \sigma_{ji}}{\partial x_j}$$

Energy:

$$\dot{e} = f_i u_i + p \dot{V} + \frac{1}{\rho} S_{ij} \dot{\epsilon}_{ij}$$

The projectile and the targets are modeled using 8-node hexahedron solid elements and using one integration point. For the projectile a butterfly mesh is used with an element size similar to the target element size in the area of impact.

For the metals material we chose the Johnson Cook model that includes damage and tensile failure [63]:

$$\sigma^0 = \left(A + B (\epsilon^p)^n \right) \left(1 + C \log \left(\frac{\dot{\epsilon}^p}{\dot{\epsilon}_0} \right) \right) \left(1 - \hat{T}^m \right)$$

with

$$\hat{T} = \begin{cases} 0 & \text{for } T < T_r \\ \frac{T - T_r}{T_m - T_r} & \text{for } T_r \leq T \leq T_m \\ 1 & \text{for } T > T_m \end{cases}$$

and ϵ^p is the equivalent plastic strain.

This model, which is the most frequently-used for finite element modeling, takes into consideration three different effects; strain hardening, viscosity and thermal softening.

The following table, *Table 4*, presents the input material parameters used for our Johnson Cook plasticity model [61, 63]:

| Material | Reference density (Kg/m ³) | Specific heat (J/KgK) | Melting temp (K) | Room temp (K) | A (MPa) | B (MPa) | n | m | c | ξ^0 (s ⁻¹) |
|-----------|--|-----------------------|------------------|---------------|---------|---------|------|------|-------|----------------------------|
| Al2024-T3 | 2.77 | 875 | 775 | 300 | 265 | 426 | 0.34 | 1 | 0.015 | 1 |
| Al6061-T6 | 2.7 | 885 | 925 | 300 | 324.1 | 113.8 | 0.42 | 1.34 | 0.002 | 1 |
| Ti-6Al-4V | 4.43 | 670 | 1903 | 300 | 862 | 331 | 0.34 | 0.8 | 0.012 | 1 |

Table 4: Johnson Cook plasticity model parameters for the metals used in simulation

Johnson Cook fracture model is used to model the fracture and element deletion. This allows comparison of the effective plastic strain with the failure strain (maximum allowed deformation of an element before it is deleted) [64, 65]:

$$\bar{\epsilon}_f = \left[D_1 + D_2 \cdot \exp(D_3 \eta) \right] \left[1 + D_4 \ln \left(\frac{\dot{\bar{\epsilon}}}{\dot{\bar{\epsilon}}_0} \right) \right] \left[1 + D_5 \left(\frac{T - T_{room}}{T_m - T_{room}} \right) \right]$$

Where D_i , $i=1$ to 5 are input constants (five failure parameters) and η is the stress triaxiality parameter (ratio of the pressure to the effective stress). Determination of the five parameters (D_i) involves a series of experimental fracture tests, which would complicate the simulation procedure and is not within the goal of this research. For our work we used pre-determined values of these parameters found in literature [57, 66], and adapted them to obtain results in agreement with the theoretical penetration limit calculated for each material case.

The projectile diameter is known, and it is necessary to determine the penetration velocities in order to calibrate our models. The following ballistics equations were used [67]:

- For Aluminium targets, the Cour-Palais semi-infinite plate equations [68] describe the impact of a spherical projectile on a semi-infinite metallic plate

$$d_c = \left[\frac{t_s}{k} \cdot \frac{HB^{0.25} (\rho_s / \rho_p)^{0.5}}{5.24 (V \cos \theta / C)^{2/3}} \right]^{18/19} \quad \text{If } (\rho_p / \rho_s) < 1.5$$

$$d_c = \left[\frac{t_s}{k} \cdot \frac{HB^{0.25} (\rho_s / \rho_p)^{3/2}}{5.24 (V \cos \theta / C)^{2/3}} \right]^{18/19} \quad \text{If } (\rho_p / \rho_s) \geq 1.5$$

- For Titanium targets, the same equations are slightly modified [69]

$$d_c = \frac{t_s}{k} \cdot \frac{HB^{0.25} (\rho_s / \rho_p)^{0.5}}{5.24 (V \cos \theta / C)^{2/3}}$$

- For carbon fiber reinforced plastic (CFRP), crater formation and shock transmission in multilayer is different to that in metals. We used a Schaefer [70] modified equation which includes a single empirically-determined material parameter (K_{CFRP}) to represent the material properties

$$d_c = \frac{t_s (\rho_s / \rho_p)^{0.5}}{k \cdot K_{CFRP} \cdot (V \cos \theta)^{2/3}}$$

- For honeycomb panels, we used the Schaefer Ryan Lambert (SRL) triple-wall BLE [71,72] for the low velocity range (up to 3 km/s)

$$d_c = \left[\frac{t_w / K_{3S} \cdot (\sigma / 40)^{1/2} + t_b}{0.6 (\cos \theta)^\delta \rho_p^{1/2} V^{2/3}} \right]^{18/19}$$

Where:

d_c – projectile diameter, for the ballistic limit (cm)

t_s - target (shield) thickness (cm)

HB - Brinell hardness (HB)

k - failure coefficient, for perforation equal to 1.8

V - projectile velocity (km/s)

ρ - density (g/cm³), p- projectile, s- target

θ - impact angle measured from the target normal to velocity vector (radians)

K_{CFRP} – material constant = 0.62

K_{3S} - low-velocity coefficient, 1.4 for Al facesheets and 1.1 for CFRP

t – facesheet thickness (cm), b- bumper, w – rear wall

σ - Rear wall yield stress (ksi) (Note: 1 ksi = 1,000 lb/in² = 6.895 MPa)

δ – a constant function of impact angle, 4/3 for Al and CFRP at normal impact angle

C – speed of sound.

The following tables summarize the main properties and dimensions of materials used in simulation.

| Material | Density (g/cm ³) | Yield strength (ksi) | Sound Speed (km/s) | Brinell hardness (HB) |
|--------------------|------------------------------|----------------------|--------------------|-----------------------|
| Al 6061-T6 | 2,7 | 40 | 5,05 | 95 |
| Al 2024-T4 | 2,77 | 47 | 5,11 | 120 |
| Ti-15V-3Cr-3Al-3Sn | 4,73 | 181 | 4,26 | 257 |
| CFRP | 1,38-1,85 | 59,5 | | |
| Ti-6Al-4V | 4,43 | 128 | | 334 |

Table5: Simulation materials mechanical properties

| Type | Material | Diameter (cm) | Thk (cm) |
|------------------|-----------|---------------|----------|
| Projectile | Al2024-T4 | 0,3175 | |
| Target | Al6061-T6 | | 0,4826 |
| Target | Al6061-T6 | | 0,08128 |
| Target | CFRP | | 0,3175 |
| Target | Titanium | | 0,08128 |
| HC/SP facesheets | Al6061-T6 | | 0,08128 |
| HC/SP facesheets | CFRP | | 0,15875 |

Table 6: Projectile and target dimensions

Using the material characteristics, dimensions and the ballistic equations described above we obtained the following results.

| Material | Thk. (cm) | Projectile diam (cm) | Perforation Vel. (Km/s) |
|------------|-----------|----------------------|-------------------------|
| Al6061-T6 | 0,08128 | 0,3175 | 0,13445481 |
| Al6061-T6 | 0,4826 | 0,3175 | 1,945278452 |
| Al6061-T6 | 0,3175 | 0,3175 | 1,03804551 |
| Ti-15V | 0,08128 | 0,3175 | 0,227968483 |
| Ti- 6Al | 0,08128 | 0,3175 | 0,401085717 |
| Ti-15V | 0,15 | 0,3175 | 0,571526214 |
| Ti- 6Al | 0,15 | 0,3175 | 0,704585179 |
| CFRP | 0,3175 | 0,3175 | 0,561996833 |
| CFRP | 0,15875 | 0,3175 | 0,198695886 |
| HC/SP-Al | 0,08128 | 0,3175 | 0,320567441 |
| HC/SP-CFRP | 0,15875 | 0,3175 | 0,898928919 |
| HC/SP-CFRP | 0,145 | 0,3175 | 0,799914848 |

Table 7: Calculated velocity for the proposed materials

HVI simulations

Introduction

As previously mentioned at the end of *Chapter 1*, we performed LS-DYNA impact simulations for materials of each of the groups in order to identify distinct characteristics of the impact.

The projectile characteristics are the same for all simulations; Al 2024- T4 is the material and the projectile diameter is 0.3175 cm.

All targets are square rigid sheets, 12 cm x 12 cm fixed around all four edges.

The resultant acceleration is captured at a distance of 3.5 cm from the impact.

Aluminium

In order to have a better understanding of impact characteristics, two target thicknesses were used; 0.08128 and 0.3175 cm. Target material was Al 6061-T6 alloy. For the 0.08128 cm thickness, impact velocities were 0.1 km/s, 0.14 km/s and 0.3 km/s. Screen shots of the impacts are presented in *Figure 3*.

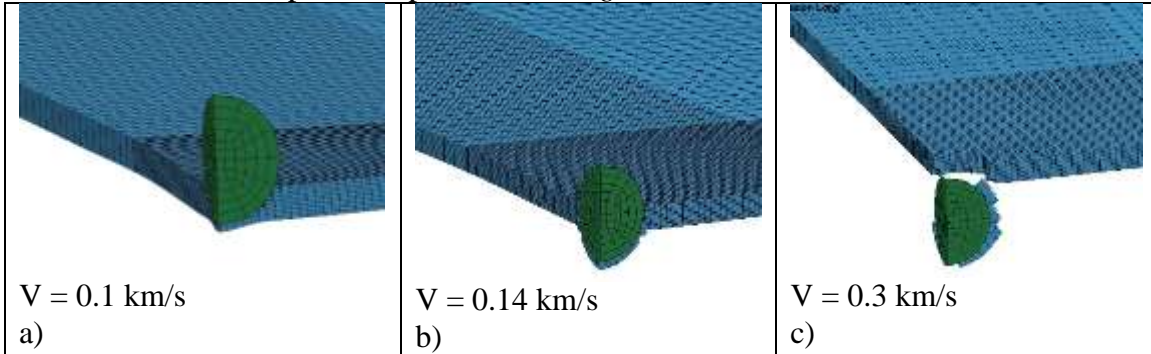
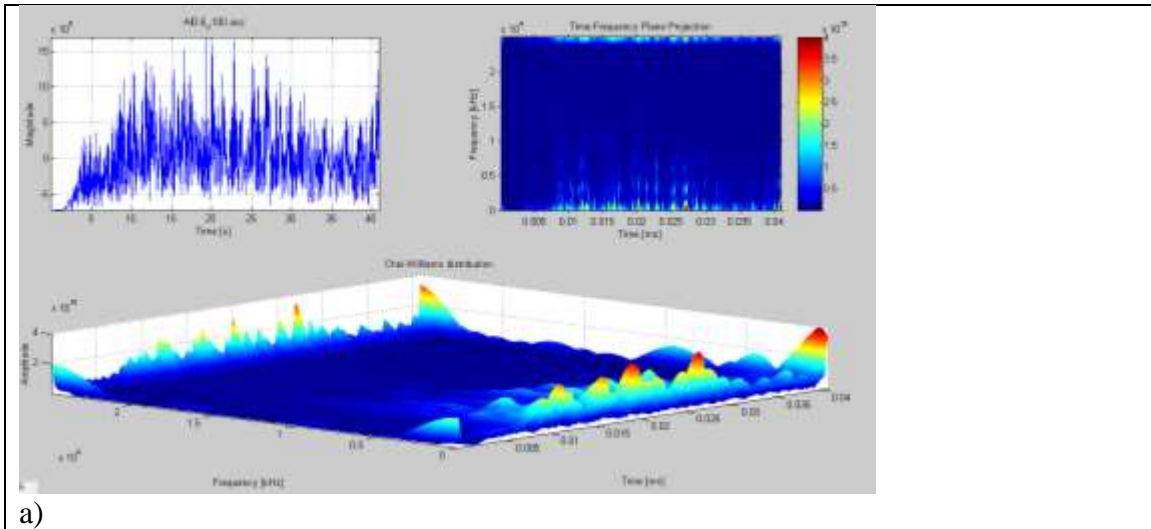


Figure 3: Impact simulation on an Al plate of 0.08128 cm thickness: a) non-penetration; b) penetration occur/penetration limit; c) full penetration.

The time-frequency analysis Choi-Williams distribution (CWD) shows the following results for the three different velocities. Three types of damage can be identified: a back-face bump, occurrence of cracks/penetration limit and perforation, *Figure 4*.



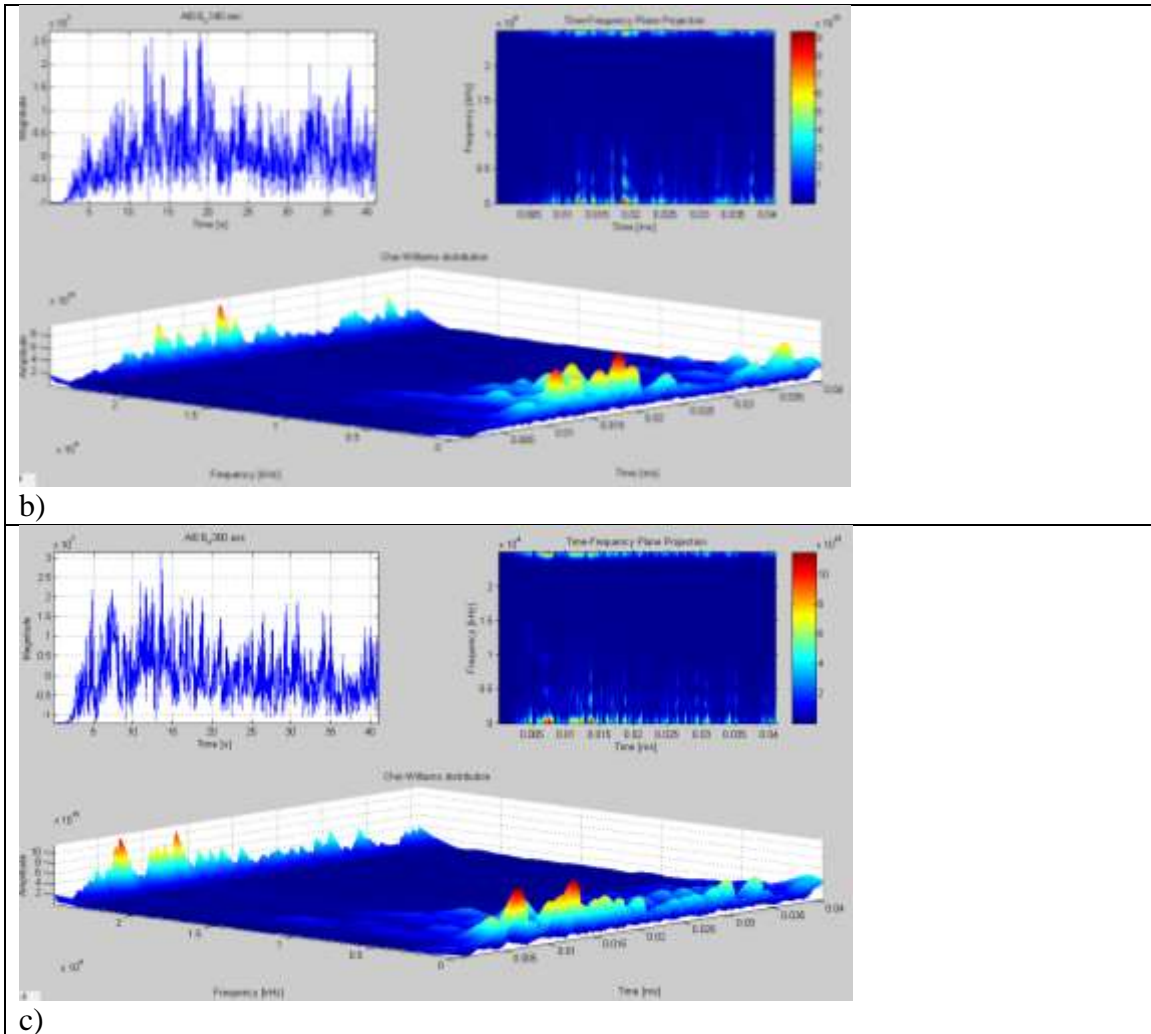


Figure 4: CWD for impact on Al6061-T6 of 0.08128 cm thickness: a) non-penetration; b) penetration limit; c) full penetration.

The CWD shows that, in the case of a thinner Al target (0.8128 cm thk.) in the non-penetration state (a) a series of frequency peaks occur with amplitudes between 2 to 4×10^{15} in a time range of 0.01 to 0.03 ms. The sensor recorded the first impact wave group, which was followed by different waves reflected back from the lateral edges

At the penetration limit (b) the frequency amplitude is higher and more compact on a 0.01 ms time interval. This interval is even smaller in the case of full penetration (c) and two individual frequency peaks of 10×10^{15} become apparent. These could represent the different impact waves that were captured by the sensor at the moment of impact on the front and back face. In the same moment a series of smaller accentuated frequency peaks are present at the limit of penetration (b)

Identification of the origin of the frequency peaks is not the object of our work. The study of impact wave behavior is a complex process. Some work in this area has been done by Betella [73].

In order to confirm a specific form of the penetration on Al plates a second simulation was made on a thicker target using the same projectile characteristics.

The second target is a 0.3175 cm Al plate. Impact velocities were 0.7 km/s, 0.9 km/s and 1.1 km/s. Screen shots of the impact can be seen in *Figure 5*.

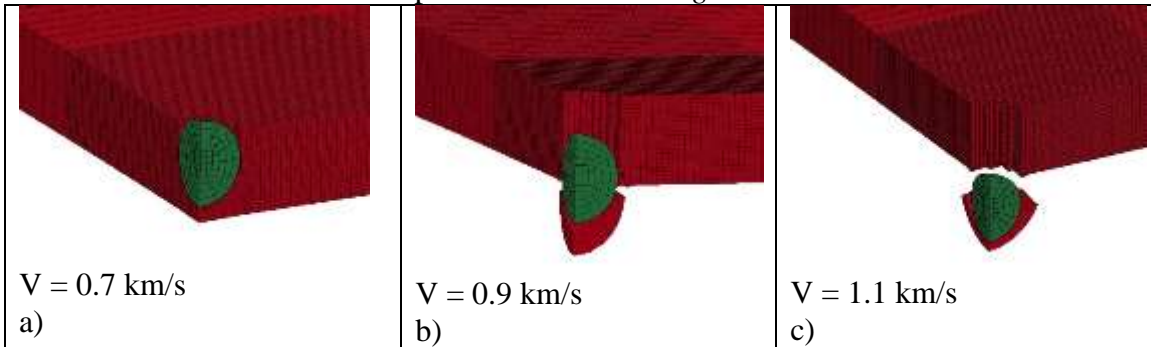
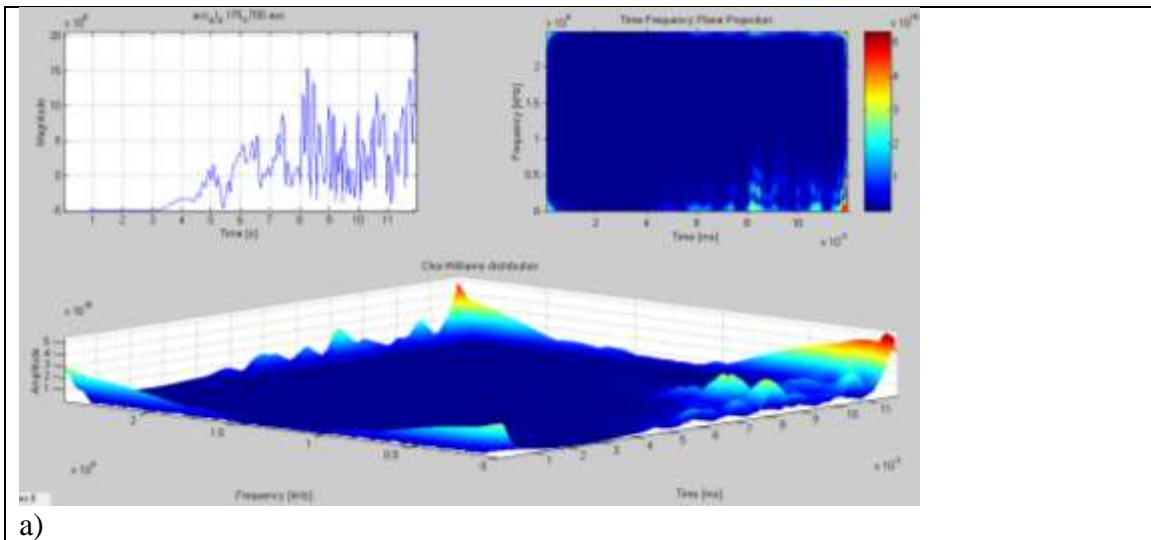


Figure 5: Impact simulation on an Al plate of 0.3175 cm thickness: a) non-penetration; b) penetration occur/penetration limit; c) full penetration.

The CWD with the corresponding three types of damage are presented in the following figure, *Figure 6*.



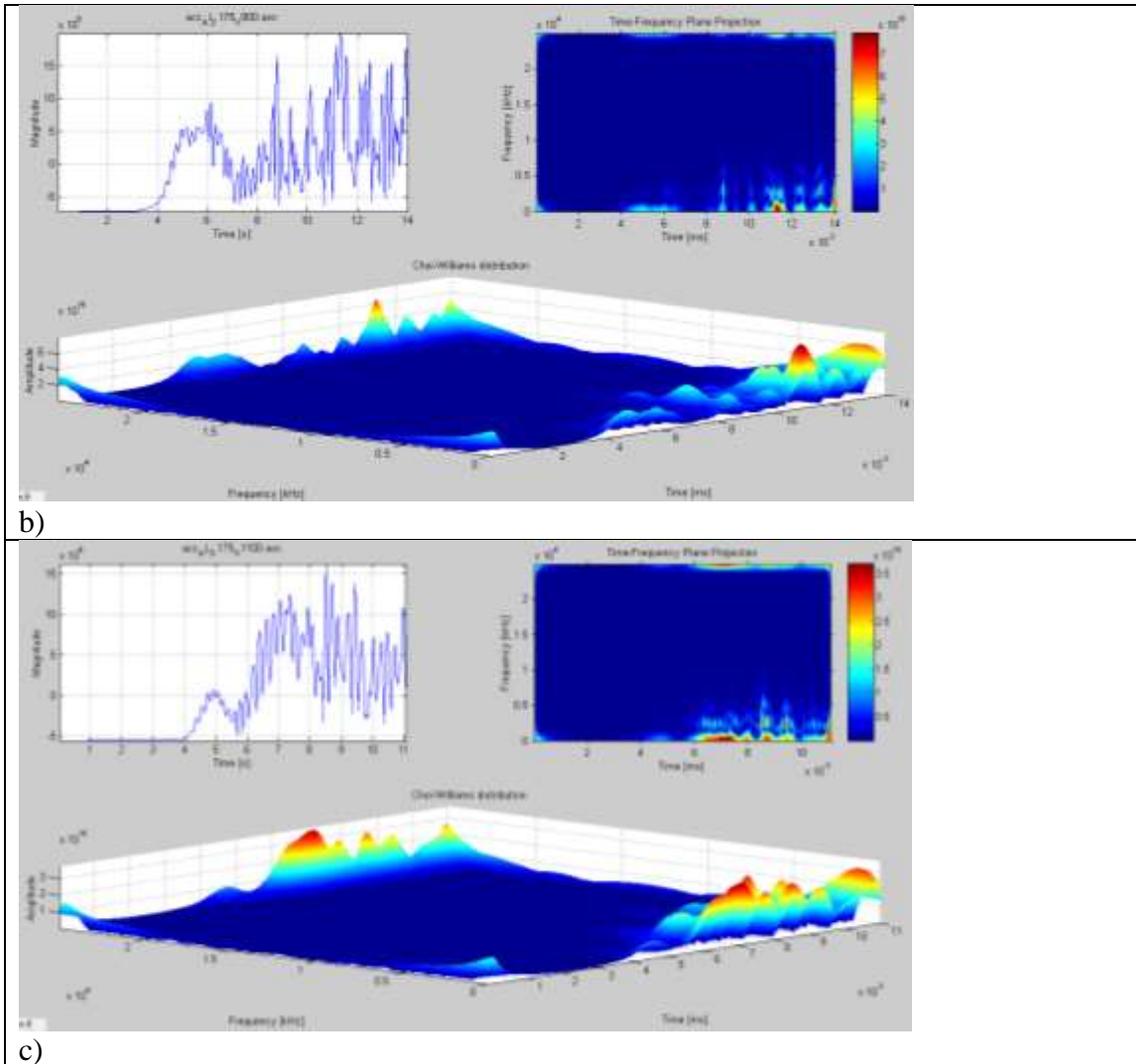


Figure 6: CWD for impact on Al6061-T6 of 0.3175 cm thickness: a) non-penetration; b) penetration limit; c) full penetration.

For this plate the same non-penetration characteristics are shown on the CWD (a), a series of frequency peaks occur. Peaks with amplitudes between 1.5 to 5×10^{15} in a time interval of $5 \mu\text{s}$. Both peaks exhibit a slight contour.

The following two states show the corresponding two peaks that define penetration. In the case of full penetration (c), the first peak is more accentuated and reaches a higher frequency amplitude, around $3 - 4 \times 10^{15}$.

These simulation results are in good agreement with previously mentioned experimental tests [74]. The large frequency peaks profile recorded for the non-penetration case in the experimental session correspond to the series of frequency peaks obtained in our simulation. Another good correlation between the simulation and testing session was noticed at the level of frequency amplitude for the case of non-penetration on the thicker plate. This amplitude is almost half that obtained for the case of penetration of the thinner target.

The sensor used for the experimental session was not specifically designed for hypervelocity impact; since wave velocities are high the frequency modification and traveling time of the impact wave is very small (μs).

Titanium

Titanium is the second metal from the first group of materials used in manufacture of spacecraft. Simulations were carried out using the characteristics of this material in order to have a better analysis of impact and to understand the characteristics of the three types of damage. For our impact model we used Ti-6Al-4V, which is widely used in the aerospace industry and already implemented in LS-Dyna.

We used a 0.08128 cm thickness Ti plate. Impact velocities were 0.4 km/s, 0.5 km/s and 0.7 km/s. A capture of the impact is presented in *Figure 7*.

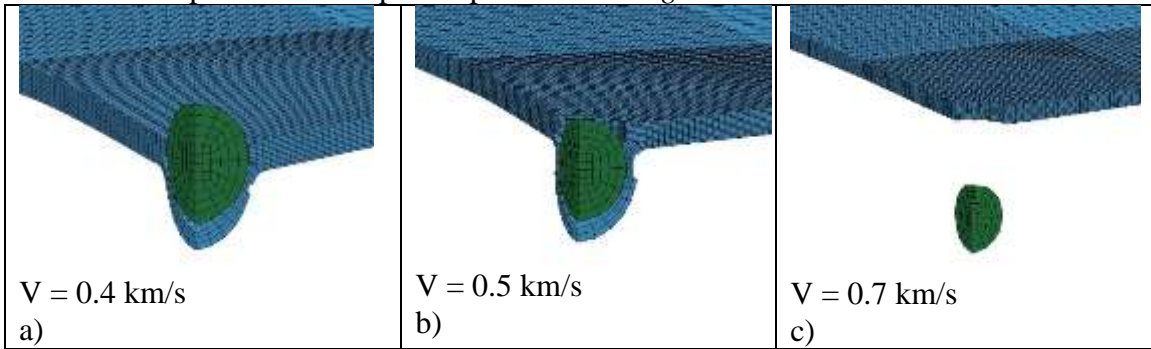
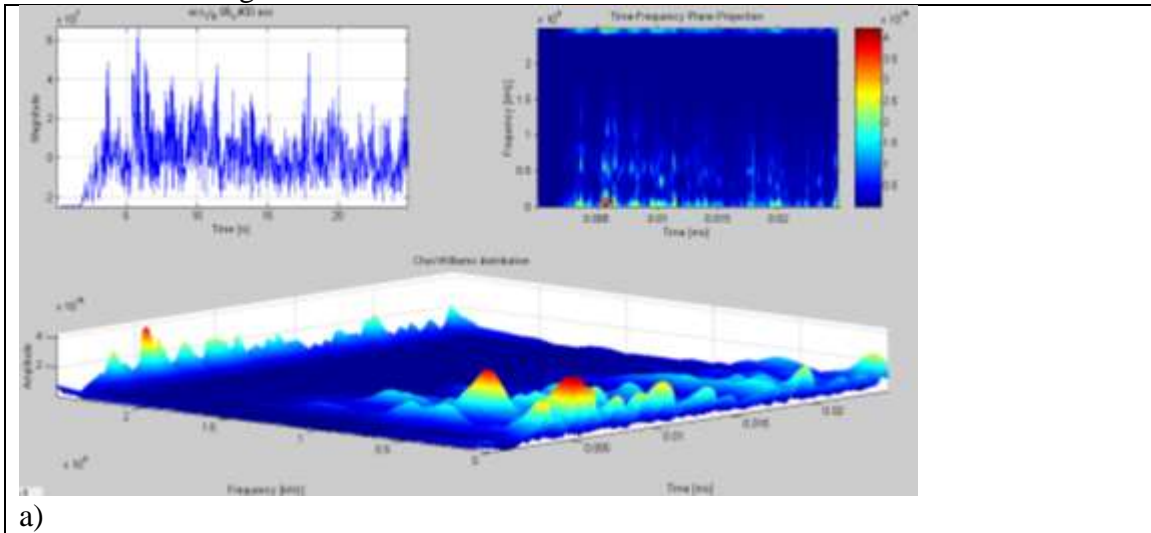


Figure 7: Impact simulation on Ti plate of 0.08128 cm thickness: a) non-penetration; b) penetration occur/penetration limit; c) full penetration.

The following figure, *Figure 8*, shows the CWD for the three types of damage that occurred on the titanium target



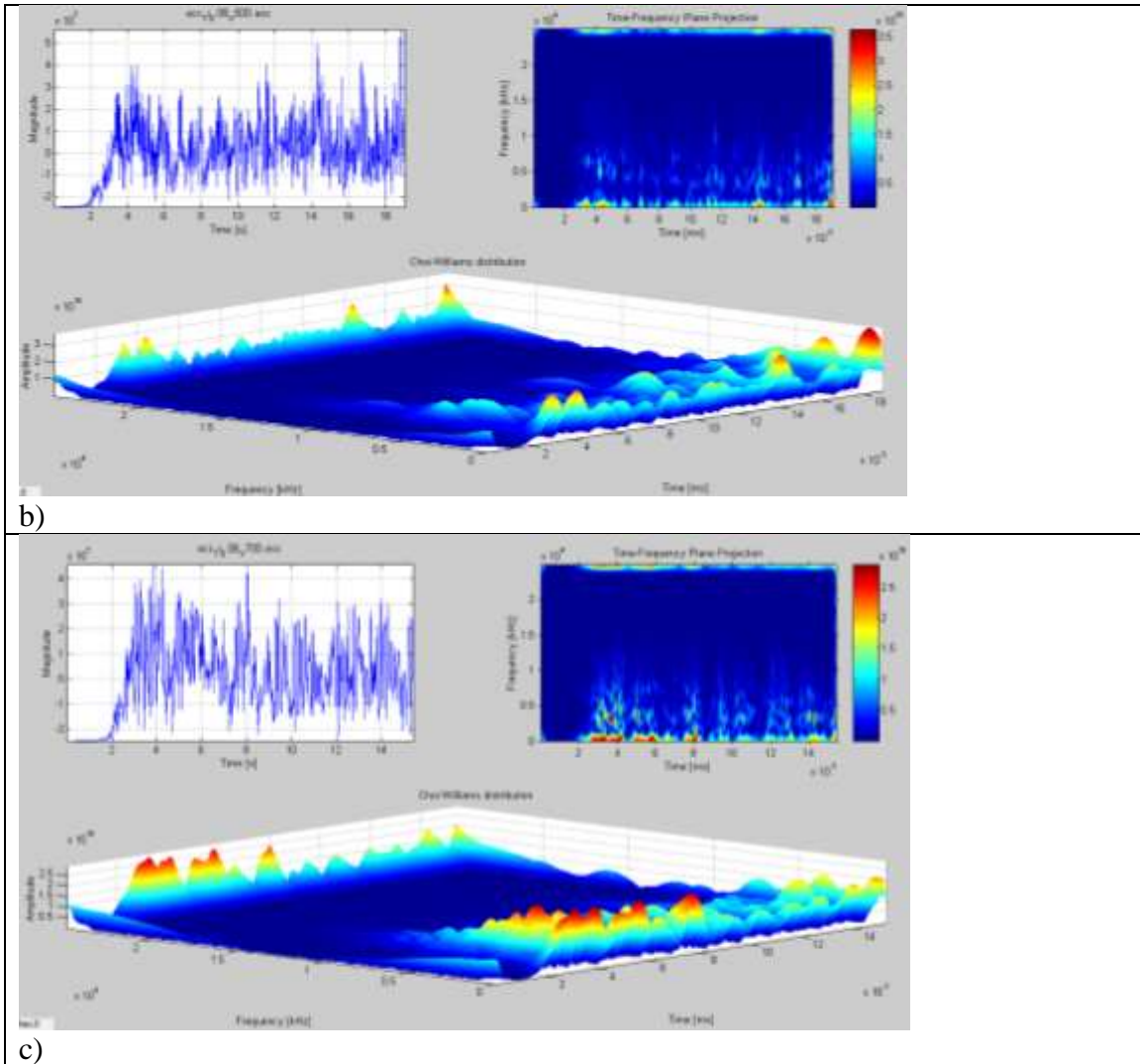


Figure 8: CWD for impact on a Ti-6Al-4V target of 0.08128 cm thickness: a) non-penetration; b) penetration limit; c) full penetration.

The simulations of impact on titanium plate exhibit a series of similarities with the aluminium simulations. For example the same multitude of frequency peaks occur for the case of penetration (c).

In the no-penetration case (a), a more accentuated frequency peak is recorded with an amplitude of 4 to 5×10^{16} . One particularity for the titanium target is the occurrence of a different frequency value at the recorded peak. Also, for this case we notice a second peak that occurs at the moment of initial impact after $5 \mu\text{s}$.

The next two cases, penetration limit (b) and full penetration (c), exhibit the same multitude of frequency peaks at different moments of impact. This appears to be characteristic of Ti targets.

At the moment of full penetration (c) the series of multiple frequency peaks are more accentuated and the peaks seem to group around two or three time moments. A similarity is again noticed with the testing session results; the frequency amplitude of the peaks in

the case of penetration is almost half the value recorded for the non-penetration case (a), at a maximum amplitude value of 2.5×10^{16} .

CFRP

For the CFRP target model we used high-strength lightweight carbon fiber, square rigid sheets of 0.3175 cm thickness.

As a mode, a simple bi-directional CFRP was used with all the fibers oriented in the 0° and 90° directions. The result is a CFRP panel with high longitudinal stiffness and lower torsional stiffness, *Figure 9*.

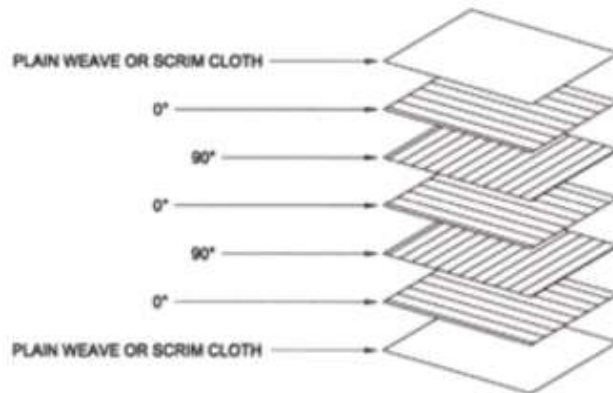


Figure 9: Schematics of the fiber layers for one half of the bi-directional CFRP model. The impact velocities on CFRP were 0.6 km/s, 0.8 km/s and 1 km/s. A capture of the impact is presented in *Figure 10*.

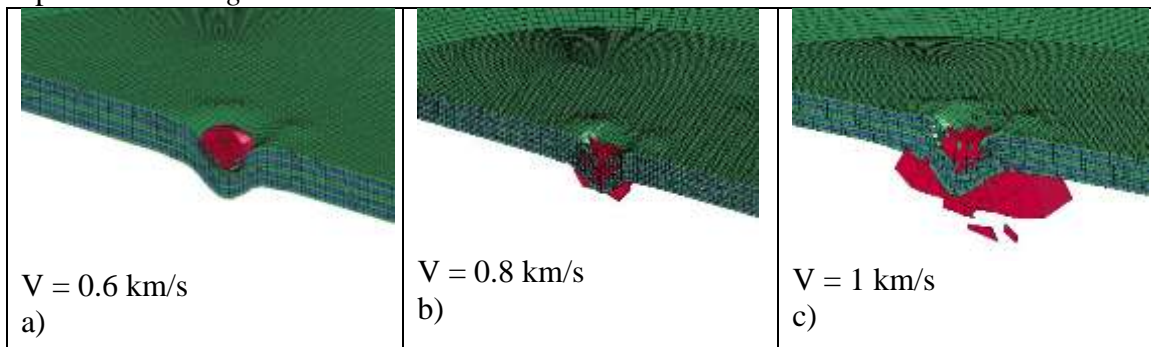


Figure 10: Impact simulation on a CFRP plate of 0.3175 cm thickness: a) non-penetration; b) penetration occur/penetration limit; c) full penetration.

The following figure, *Figure 11*, shows the CWD for the three types of damage that occurred on the CFRP target.

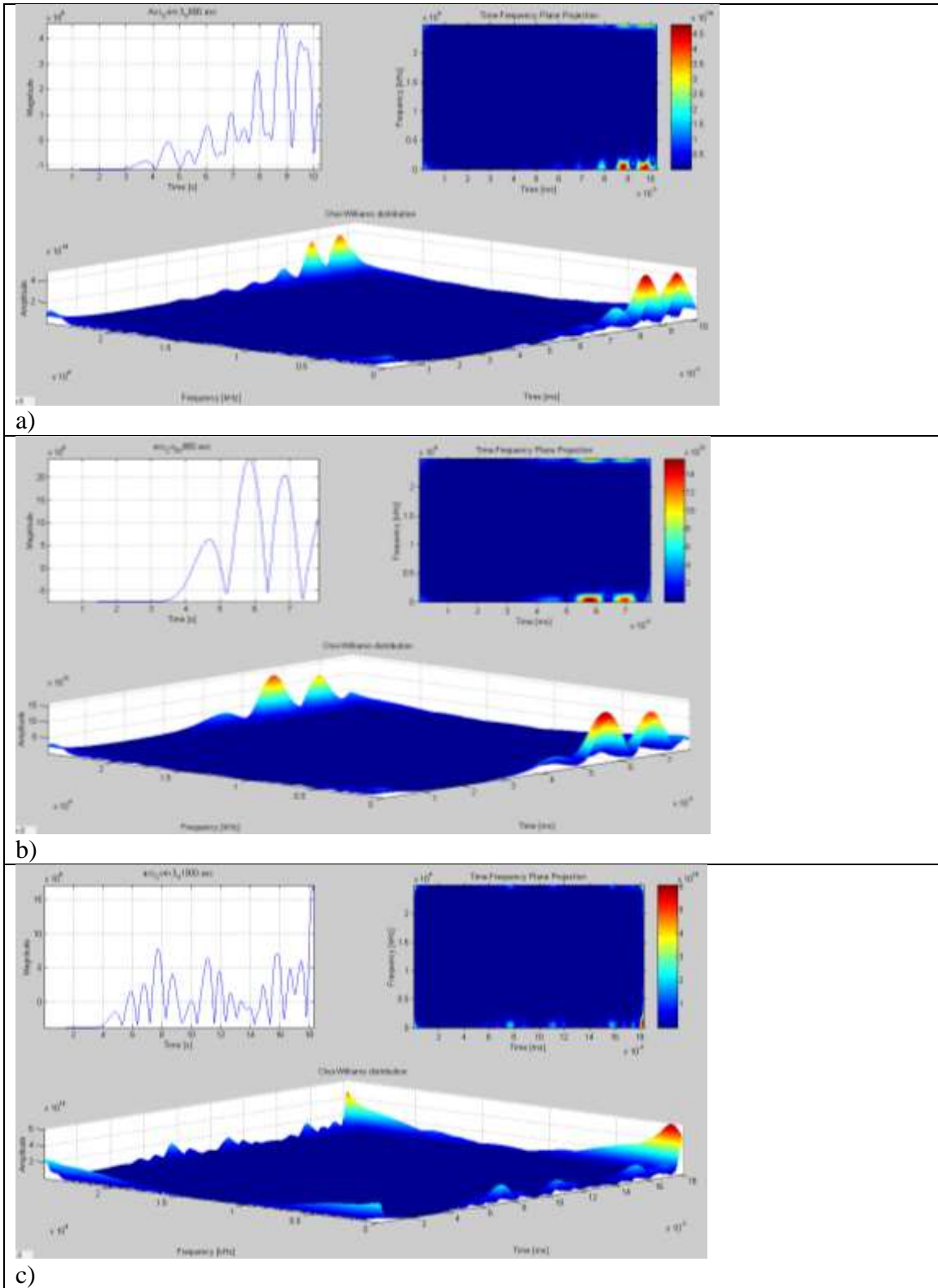


Figure 11: CWD for impact on a CFRP plate of 0.3175 cm thickness: a) non-penetration; b) penetration limit; c) full penetration.

Due to the characteristics of the material, very little variation in the acceleration was recorded during impact simulation on the CFRP target.

The CWD for the first case of non-penetration (a) shows two very clean frequency peaks at amplitude 4×10^{14} , each of them with their maximum value in the range of 0.5 μ s. A few very small frequency peaks (increasing in amplitude) occur prior to this moment.

The penetration limit (b) signal analysis shows the same two main frequency peaks but the interval on the maximum values is much larger, up to 1 μ s. The same characteristics common to penetration damage can be seen. A decrease in frequency amplitude for the second case (b) is seen, the value of this amplitude is 1.5×10^{14} .

The penetration case (c) shows three frequency peaks of maximum amplitude value 2×10^{15} . These are not well represented, probably because the final period of the simulation shows the impact of a fragment cloud on the target. This fact is not representative of the characteristics of impacts occurring after penetration is complete.

Honeycomb panels

Honeycomb panels with Al or CFRP facesheets and Al honeycomb as a material structure are often used for satellites. They are included in this work as an example of the third group of spacecraft materials. In order to simulate and analyze the impact the HC/SP can be characterized as a dual or triple wall shield structure. In this manner, we use signal analysis of AL or CFRP or analyze the acceleration obtained and considering this material as a spacecraft "material" category.

Due to the increased complexity in modeling the HC/SP, and particularly in modeling the interaction between facesheet and honeycomb material, signal analysis of impacts on HC panels will be the object of future work.

Analysis summary and discussions

The following table, *Table 8*, presents a summary of HVI simulations made in the low-velocity range on aluminium, titanium and CFRP, all of which are frequently-used materials for satellite structures.

| Material, thickness (cm) | Damage type a)Non-penetration b)Penetration limit c) Full penetration | Frequency amplitude | Shape of the signal, frequency in time and amplitude variation |
|--------------------------------------|---|----------------------------|---|
| Al 6061 –T6 0.08128 See Fig. 3 | a | 4×10^{15} | Few dispersed peaks concentrated around 2 – 3 max frequencies |
| | b | 8×10^{15} | More grouped peaks |
| | c | 10×10^{15} | Fewer peaks concentrated |
| Al 6061 –T6 | a | 5×10^{15} | Few frequency peaks |

| | | | |
|-----------------------------------|---|----------------------|---|
| 0.3175 See Fig. 5 | b | 6×10^{15} | Increase in the no. of peaks |
| | c | 3×10^{15} | Multiple peaks, max frequency larger in time |
| Ti-6Al-4V 0.08128 See Fig.7 | a | 4×10^{16} | Few peaks, variation in frequency |
| | b | 3×10^{16} | Increase in the no of peaks |
| | c | 2.5×10^{16} | Multiple peaks, variation in time and frequency |
| CFRP 0.3175 See Fig 10 | a | 4×10^{14} | Three main peaks |
| | b | 1.5×10^{14} | Three main peaks + max frequency on a larger time range |
| | c | 2×10^{15} | Three main peaks + Multiple peaks |

Table 8: Summary of CWD analysis on type of damage.

The summary table provides a clear indication of the two factors that are related to penetration; the shape/form of the recorded signal and the variation of frequency amplitude. The frequency amplitude decreases for the case of penetration or at penetration limit. As impact velocity increases this amplitude will increase again for aluminium (thick plate), titanium and CFRP. Also, it seems that the value of the decrease in frequency amplitude is half the value of the non-penetration amplitude. But again, the frequency amplitude is related to the impact velocity. A particular case is represented by the thinner aluminium plate, which shows no decrease in amplitude. This behaviour can be attributed to the small variations in velocities that tend to increase the frequency amplitude.

The second indication of penetration is the form of the signal. For all cases of penetration an increase in the number of frequency peaks is noted. Titanium, the strongest material, presents the largest number of peaks in time and also in the frequency range. The LS-Dyna simulation model we used is limited due to software and time constraints and could be improved to be better suited for modeling hypervelocity impacts, not only in the lower velocity regime but also in higher velocity regimes where phase transformations of materials occur. Calibration of the model was based only on theoretical calculations of the penetration velocities. Further calibration of models should include a series of experimental testing.

The simulation results clearly showed that, based on accelerations obtained during a series of impact simulations, different distinct penetration characteristics can be identified for each of the materials studied. The in-house TF-Analysis software was adequate to reveal this distinction. All of the materials studied are frequently used in current satellite structures.

This research definitely provides the premise that could lead to automation of the process and the creation of a viable real-time impact health monitoring system for satellites that is capable of identifying penetration due to high velocity impact of micrometeoroids and space debris for an extensive database of materials.

CONCLUSIONS AND FUTURE WORK

This work presents the HVI simulation portion of an overall research project which has been undertaken to achieve a specific goal: development of a real-time detection tool capable of quantifying the damage created by micrometeoroid and orbital debris impacts on a spacecraft. The impact simulations were made using a student version of LS-Dyna software, a general-purpose finite element program capable of simulating transient dynamics problems, which are typically encountered when simulating hypervelocity impacts.

In order to select the materials for our simulations, an extensive review was made of the types of materials that are used in the manufacture of spacecraft. This review led to the identification of three main material groups. Representatives of these groups were studied during our simulations. Due to time constraints and complexity of the model, simulations on a material from the third group, sandwich panel materials, were not made. This will be studied in a future work.

Hypervelocity impact simulations were performed on targets made of aluminum (two different thicknesses; 0.08128 and 0.3175 cm), titanium (0.08128 cm) and CFRP (0.3175 cm). The resulting accelerations were captured using a virtual sensor mounted 3.5 cm from the point of impact on the back face of the target. All targets were square rigid plates 12cm x 12cm fixed around all four edges.

The resulting acceleration signals were further analyzed using TF-Analysis software developed in-house. This software offers a wide range of analysis methods. This Time-Frequency analysis of signals was carried out using the Choi –Williams distribution method, a method that has been previously used in literature to analyze impact vibrations [75, 76].

Time-Frequency analysis clearly shows that, for aluminium, titanium and CFRP materials, amplitude of the frequency signal decreases upon occurrence of perforation. At the same time the form of the CWD is different for each type of material. For aluminium, a decrease in amplitude from $5-6 \times 10^{15}$ to 3×10^{15} is seen in the case of perforation. For titanium the amplitude drops from 4×10^{16} to $2-2.5 \times 10^{16}$, and for CFRP it decreases from $3-4 \times 10^{14}$ to 1.5×10^{14} . These values are also an indication of the rigidity of these materials. Titanium, the most rigid material simulated, exhibits a frequency amplitude (in the case of penetration) 100 times higher than CFRP. The value of frequency amplitude obtained using the time-frequency analysis also indicates the most resistant material to impact (in correlation with the perforation velocities).

The second particular characteristic for each material is the form of the CWD in the case of penetration. Although all materials showed a multiplication of the frequency amplitude peaks upon perforation, each capture exhibits different forms. The penetration of aluminium showed multiple peaks grouped together on a shorter time interval. The

maximum intensity of the frequency is largest, up to 2 μ s. For the penetration of titanium the time interval of the frequency peaks is largest with the most obvious frequency variations. The perforation of CFRP shows the smallest number of frequency peaks (approximately three frequency peaks).

The simulation results are in good agreement with measurements previously made during HVI tests [74, 77]. Using a sensor, not necessarily fit for HVI, these experimental test results showed the same decrease in frequency amplitude for the case of penetration, up to half of the maximum amplitude. The highest frequency amplitude recorded was higher for the most rigid material, and had a unique, particular shape of CWD for each material tested. These two results obtained independently, from numerical simulation and physical tests are clearly an indication that a material database can be established for each of materials from the groups identified at the end of the Chapter 1. However, a larger number of HVI tests are necessary together with the refinement of the simulation model.

Further investigation in this direction is needed, but this proposed work represents only a starting point towards automatic classification of different types of impact damage (especially perforation) on different materials. This can be done by processing images using Fourier descriptors and neural networks, with the end goal of creating a real-time micrometeoroid and space debris health monitoring system.

Completion of future work requires a larger number of simulations and HVI tests. For HVI tests, an increase in velocity of testing is needed to cover medium and high impact velocity ranges. The choice of the test facility will influence the quality of results. Ideally, we need to eliminate the second impact from the sabot, improve the acquisition system, and improve the sensing method. These improvements will lead to better results that will also help in calibrating the simulation model.

For HVI simulation in the higher velocity regime the use of SPH is highly recommended in order to capture the phase transformation of the material from solid to liquid and vapor and to obtain a signal that closely mimics the reality of HVI.

Further development of the TF-Analysis software [78, 79] will also be needed for more efficient extraction of the features of the HVI signals and to create results that are more user-friendly and compatible with other specific software.

The most important result of this work is that the use of Time-Frequency analysis in identifying HVI damage for different types of materials opens the door for other research, ultimately leading to the automation of HVI damage detection on spacecraft.

ACKNOWLEDGMENT

This research work has been made possible by precious support of a collaborative research and development grant from the Natural Sciences and Engineering Research Council of Canada (NSERC)(No.8482) and the Fonds de recherche du Québec - Nature et technologies (FRQNT).

REFERENCES

1. William P. Schonberg, Protecting earth-orbiting spacecraft against micro-meteoroid/orbital debris impact damage using composite structural systems and materials: An overview, *Advances in Space Research* 45 (2010) 709–720
2. Schonberg, W.P, Hypervelocity impact response of spaced composite material structures. *Int. J. Impact Eng.* 10, 509–, 1990.
3. Schonberg, W.P., Walker,E.J., Use of composite materials in multi-wall structures to prevent perforation by hypervelocity projectiles. *Compos. Struct.* 19, 15–, 1991.
4. Roberto Destefanis, Frank Schäfer, Michel Lambert, Moreno Faraud, Eberhard Schneider, Enhanced space debris shields for manned spacecraft, *International Journal of Impact Engineering*, Volume 29, Issues 1–10, December 2003, Pages 215–226
5. Wan, H; Bai, SX; Li, S; Mo, JJ; Zhao, SC; Song, ZF, Shielding performances of the designed hybrid laminates impacted by hypervelocity flyer, *MATERIALS & DESIGN*, 12/2013, Volume 52
6. G. S. Guan, Q. Bi, Y. Zhang, "Research of Performance about Ceramic Coating on Aluminum Bumper to Resist Hypervelocity Impact", *Key Engineering Materials*, Vols 577-578, pp. 629-632, Sep. 2013
7. Gong, WW; Liu, Y; Zhang, X; Ma, HL, Numerical Investigation on Dynamical Response of Aluminum Foam Subject to Hypervelocity Impact With Material Point Method, *CMES-COMPUTER MODELING IN ENGINEERING & SCIENCES*, 02/2012, Volume 83, Number 5
8. Ma, ZT; Bin, J; Pang, BJ, Behavior of aluminum foams under hypervelocity impact: Validation of numerical simulation, *ADVANCED ENGINEERING MATERIALS*, 10/2007, Volume 9, Numéro 10
9. Ping Liu, Yan Liu, Xiong Zhang, Internal-structure-model based simulation research of shielding properties of honeycomb sandwich panel subjected to high-velocity impact, *International Journal of Impact Engineering*, Volume 77, March 2015, Pages 120–133
10. E.A. Taylor, M.K. Herbert, B.A.M. Vaughan, J.A.M. McDonnell, Hypervelocity impact on carbon fibre reinforced plastic/aluminium honeycomb: comparison with Whipple bumper shields, *Int J Impact Eng*, 23 (1) (1999), pp. 883–893
11. E.A. Taylor, J.P. Glanville, R.A. Clegg, R.G. Turner, Hypervelocity impact on spacecraft honeycomb: hydrocode simulation and damage laws, *Int J Impact Eng*, 29 (1–10) (2003), pp. 691–702
12. R.J. Turner, E.A. Taylor, J.A.M. McDonnell, H. Stokes, P. Marriott, J. Wilkinson, et al., Cost effective honeycomb and multi-layer insulation debris shields for unmanned spacecraft, *Int J Impact Eng*, 26 (1–10) (2001), pp. 785–796
13. J.-M. Sibaud, L. Thamie, C. PUILLET, Hypervelocity impact on honeycomb target structures: Experiments and modeling, *International Journal of Impact Engineering* 35 (2008) 1799–1807
14. S. Ryan, T. Hedman,, E.L. Christiansen, Honeycomb vs. foam: Evaluating potential upgrades to ISS module shielding, *Acta Astronautica* Volume 67, Issues 7–8, October–

November 2010, Pages 818–825

15. Colombo, P., Arcaro, A., Francesconi, A., Pavarin, D., Rondini, D., Debei, S. Effect of hypervelocity impact on microcellular ceramic foams from a preceramic polymer. *Adv. Eng. Mater.* 5(11), 802–805, 2003.

16. Pilseong Kang, Sung-Kie Youn, Jae Hyuk Lim, Modification of the critical projectile diameter of honeycomb sandwich panel considering the channeling effect in hypervelocity impact, *Aerospace Science and Technology*, Volume 29, Issue 1, August 2013, Pages 413–425

17. William Schonberg, Frank Schäfer, Robin Putzar, Hypervelocity impact response of honeycomb sandwich panels, *Acta Astronautica*, Volume 66, Issues 3–4, February–March 2010, Pages 455–466

18. J. Warren, M. Cole, et al., “Hypervelocity impact of honeycomb core sandwich panels filled with shear thickening fluid”, 28th Technical Conference of the American Society for Composites, State College, 2013

19. Eldon P. Kasl, Lessons Learned in Modular Bus Structure Development for the LADEE Mission, *Reinventing Space Conference* October 14-17, 2013, Los Angeles, CA

20. S. Ryan, F.K. Schaefer, R. Destefanis, M. Lambert, A ballistic limit equation for hypervelocity impacts on CFRP/Al HC satellite structures, *Advances in Space Research*, 41 (2008), pp. 1152–1166

21. Thompson, T. C., Grastataro, C., Smith, B. G., Krumweide, G. and Tremblay, G., Development of an all-composite spacecraft bus for small satellite programs. In *Proceedings from The Eighth Annual AIAA/USU Conference on Small Satellites*, Logan, UT, 1994

22. M. Nicoletto, D. Boschetti, P. Savi, High Speed Digital Lines routed on non-metallic Spacecraft structures, *Proc. of the 2014 International Symposium on Electromagnetic Compatibility (EMC Europe 2014)*, Gothenburg, Sweden, September 1-4, 2014

23. Changqing, Miao; Bo, Liu, Experimental Study on the Behavior of a New Multilayer Shield Against Hypervelocity Debris Impact, *Polymers & Polymer Composites* 22.2 (2014): 99-103.

24. Offenberger, Sean; Warren, Justin; Lacy, Thomas E.; Ostaz, Ahmed Al; Toghiani, Hossein; Kundu, Santanu; Pittman Jr., Charles U.; Li, Xiaobing; Mansrah, Al-Harith, Novel composite shielding concepts for hypervelocity orbital debris impact mitigation, *55th AIAA/ASME/ASCE/AHS/SC Structures, Structural Dynamics, and Materials Conference*

25. Aleksandr Cherniaev, , Igor Telichev, Meso-scale modeling of hypervelocity impact damage in composite laminates, *Composites Part B: Engineering*, Volume 74, 1 June 2015, Pages 95–103

26. Q. Guo, D.L. Sun, L.T. Jiang, X.L. Han, G.Q. Chen, G.H. Wu, Residual microstructure associated with impact craters in TiB₂/2024Al composite, *Micron* Volume 43, Issues 2–3, February 2012, Pages 344–348

27. A.H. Baluch, C.G. Kim, J.B. Moon, and G. Lim, BEHAVIOR OF CARBON-EPOXY COMPOSITE FOR HYPERVELOCITY IMPACTS AT OBLIQUE ANGLE ON SPACECRAFT IN LOW EARTH ORBIT ENVIRONMENT, 18th International Conference on Composite Materials. August 21-26, 2011: Jeju- Korea

28. Cheng, Wing L; Langlie, Scott; Itoh, Shigeru, High velocity impact of thick composites, *International Journal of Impact Engineering*, 2003, Volume 29, Number 1
29. B. Aïssa ; E. Haddad ; K. Tagziria ; W. Jamroz ; M. Asgar-Khan ; S. V. Hoa ; J. Verreault ; A. Higgins ; D. Therriault, Exploring self healing of CFRP laminates exposed to hypervelocity small pellets simulating space debris, 26th Annual Technical Conference of the American Society for Composites 2011 and the 2nd Joint US-Canada Conference on Composites
30. OLEG V. STARTSEV and V. V. ISUPOV, The Gradient of Mechanical Characteristics Across the Thickness of Composite Laminates After Exposure to a Low Earth Orbit Environment, *Polymer Composites*, Volume 19, Issue 1, pages 65–70, February 1998
31. Lei Wang, T. Sui, W. Lin, Fatigue damage accumulation model and fatigue life predication of composite laminate TT300/ epoxy-resin, Conference: 2011 International Conference on Advanced Materials and Computer Science, ICAMCS 2011
32. Hoffman, C.N.; Snyder, B.A. ; Dean, M.W. , Development of a composite (K1100/CE) satellite bus structure, Conference: 41. International symposium of the Society for the Advancement of Material and Process Engineering and exhibition: materials and processes challenges - aging systems, affordability, alternative applications, Anaheim, CA (United States), 25-28 Mar 1996
33. Lee Hamill, Scott Roberts, Marc Davidson, William L. Johnson, Steven Nutt and Douglas C. Hofmann, Hypervelocity Impact Phenomenon in Bulk Metallic Glasses and Composites, *ADVANCED ENGINEERING MATERIALS* 2014, 16, No. 1
34. Marc Davidson, Scott Roberts, Gerhard Castro, Robert Peter Dillon, Allison Kunz, Henry Kozachkov, Marios D. Demetriou, William L. Johnson, Steve Nutt and Douglas C. Hofmann, Investigating Amorphous Metal Composite Architectures as Spacecraft Shielding, *ADVANCED ENGINEERING MATERIALS* 2013, 15, No. 1—2
35. Douglas C. Hofmann, Lee Hamill, Eric Christiansen and Steve Nutt, Hypervelocity Impact Testing of a Metallic Glass-Stuffed Whipple Shield, *ADVANCED ENGINEERING MATERIALS*, Feb.2015
36. S. Katz, E. Grossman, I. Gouzman, M. Murat, E. Wiesel, H.D. Wagner, Response of composite materials to hypervelocity impact, *International Journal of Impact Engineering*, Volume 35, Issue 12, December 2008, Pages 1606–1611
37. Eric P. Fahrenthold, Young-Keun Park, Simulation of hypervelocity impact on aluminum-Nextel-Kevlar orbital debris shields, *International Journal of Impact Engineering*, Volume 29, Issues 1–10, December 2003, Pages 227–235
38. Grosch, Donald J, Inhibited Shaped Charge Launcher Testing of Spacecraft Shield Designs, Apr 24, 1997, Southwest Research Inst.; Materials and Structures Div.; San Antonio, TX United States
39. Richard R. Burt, Eric L. Christiansen, Hypervelocity impact testing of transparent spacecraft materials, *International Journal of Impact Engineering*, Volume 29, Issues 1–10, December 2003, Pages 153–166
40. SONG LiHong, WEI Qiang, BAI Yu & GAO Cheng, Impact effects on fused quartz glass by ground simulating hypervelocity space debris, *SCIENCE CHINA Technological Sciences*, *SCIENCE CHINA*, March 2013 Vol.56 No.3: 724–731

41. X. Huang, Z. Lina, Z.D. Liu, H.S. Zhang, L.H. Dai, Amorphous alloy reinforced Whipple shield structure, *International Journal of Impact Engineering*, Volume 42, April 2012, Pages 1–10
42. <http://materion.com/Markets/DefenseandScience/SpaceScienceandAstronomy/SpaceStructuresandSatellites.aspx>
43. Serhan Avcu, Bilgin Celd, Structural Material Selection and Processing for Low Earth Orbit Spacecraft Regarding Atomic Oxygen Effects, Conference: Recent Advances in Space Technologies, 2003. RAST '03
44. GROSSMAN, E; ELIAZ, N; GOUZMAN, I; GROUND SIMULATION OF HYPERVELOCITY SPACE DEBRIS IMPACTS ON POLYMERS, PROTECTION OF MATERIALS AND STRUCTURES FROM THE SPACE ENVIRONMENT, 2006
45. R. Verker, N. Eliaz, I. Gouzman, S. Eliezer, M. Fraenkel, S. Maman, F. Beckmann, K. Pranzas, E. Grossman, The effect of simulated hypervelocity space debris on polymers, *Acta Materialia*, Volume 52, Issue 19, 8 November 2004, Pages 5539–5549
46. Irina Gouzman, Olga Girshevitz, Eitan Grossman, Noam Eliaz and Chaim N. Sukenik, Thin Film Oxide Barrier Layers: Protection of Kapton from Space Environment by Liquid Phase Deposition of Titanium Oxide, *applied materials and interfaces*, VOL. 2, NO. 7, 1835–1843, 2010
47. A.A. Voevodin, J.S. Zabinski, Nanocomposite and nanostructured tribological materials for space applications, *Composites Science and Technology*, Volume 65, Issue 5, April 2005, Pages 741–748
48. Joo Hyun Han, Sang Eui Lee, Won Jun Lee, and Chun Gon Kim, SPACE ENVIRONMENT CHARACTERISTICS OF MWNT/EPOXY COMPOSITES, Conference: 49th International SAMPE Symposium and Exhibition: Materials and Processing Technology - 60 Years of SAMPE Progress, SAMPE 2004
49. Jae-Hwang Lee, David Veysset, Jonathan P. Singer, Markus Retsch, Gagan Saini, Thomas Pezeril, Keith A. Nelson, Edwin L. Thomas, High strain rate deformation of layered nanocomposites, *Nature Communications* vol3 (Oct 2012)
50. Francois Cardarelli, *Materials Handbook, A Concise Desktop Reference*, Springer-Verlag London, 2008
51. J. Wijker, *Spacecraft Structures*, Springer-Verlag Berlin Heidelberg, 2008
52. Annarella, C., *9 Spacecraft Structures*, 1991
53. Cour-Palais, B.G. 1986. Hypervelocity impacts in metals. *International Journal of Impact Engineering* 5:221–238.
54. Christiansen, E.L., R. Bernhard, J. Hyde, J. Kerr, K. Edelstein, J. Ortega, and J. Crews. 1993. Assessment of high velocity impacts on exposed shuttle surfaces. Pp. 447–452 in *Proceedings of the First European Conference on Space Debris*, Darmstadt, Germany, 5–7 April 1993. Darmstadt: European Space Operations Center.
55. Reimerdes, H.-G., K.-H. Stecher, and M. Lambert, Ballistic Limit Equations for the Columbus-Double Bumper Shield Concept, ESA SD-01, *Proceedings of the First European Conference on Space Debris*, Darmstadt, Germany, 1993.
56. Watts, A., D. Atkinson, and S. Rieco. 1993. Dimensional Scaling for Impact Cratering and Perforation. NASA NCR-188259. March 16, Houston, Texas: National Aeronautics and Space Administration Johnson Space Center.

57. Bennetti, A., Numerical and experimental investigation of high velocity impacts for spacecraft protection, MSc Thesis, Cranfield University, 2002.
58. Guanyu, S. Junyan, G and Chun, L., Efficient modeling of panel-like targets in perforation simulation, Third European LS-Dyna User Conference, Paris, 2001.
59. Bashurov, V. V. et al., Experimental modelling and numerical simulation of high- and hypervelocity space debris impact to spacecraft shield protection, International Journal of Impact Engineering, Vol. 20, pp. 69-78, 1977
60. IADC-04-03, PROTECTION MANUAL, Version 7.0, September 19, 2014.
61. Rade Vignjevic, James Campbell, Séverine Lepage, Numerical Simulation of High Velocity Impacts on Thin Metallic Targets I, Crashworthiness, Impact and Structural Mechanics (CISM) Cranfield University, UK, Conference paper, 2004
62. LS-DYNA. KEYWORD USER'S MANUAL. VOLUME I. May 2007. Version 971. LIVERMORE SOFTWARE TECHNOLOGY CORPORATION (LSTC)
63. Yancheng Zhang, J.C. Outeiro, Tarek Mabrouki, On the Selection of Johnson-cook Constitutive Model Parameters for Ti-6Al-4 V Using Three Types of Numerical Models of Orthogonal Cutting, Procedia CIRP, Volume 31, 2015, Pages 112–117, 15th CIRP Conference on Modelling of Machining Operations (15th CMMO)
64. Hallquist, J. O., LS-DYNA Theoretical Manual, Livermore Software Technology Corporation, 1998.
65. Johnson GR, Cook WH. A constitutive model and data for metals subjected to large strains, high strain rates and high temperatures. In: Proc. 7th Int. Symp. On Ballistics, Hague, Netherlands, April 1983; 541–547.
66. Vignjevic, R., Hughes, K. and Taylor E.A., Finite element modelling of failure of a multi-material target due to high velocity space debris impacts, Space Debris, Vol. 2, pp. 41-50, 2002.
67. Shannon Ryan, Eric L. Christiansen, Micrometeoroid and Orbital Debris (MMOD) Shield Ballistic Limit Analysis Program, NASA/TM–2009–214789.
68. B.G. Cour-Palais. “Hypervelocity Impact Investigations and Meteoroid Shielding Experience Related to Apollo and Skylab.” Orbital Debris Workshop, NASA CP-2360 (pp.247-275), Houston, August 27–29, 1982.
69. E.L. Christiansen, E Cykowski, J Ortega, “Highly Oblique Impacts into Thick and Thin Targets.” Int. J. Impact Eng., 14: 157-168, 1993.
70. F. Schaefer, E. Schneider, M. Lambert. “Review of Ballistic Limit Equations for CFRP Structure Walls of Satellites.” 5th International Symposium on Environmental Testing for Space Programmes, ESA SP-558, Noordwijk, June 15–17, 2004.
71. S. Ryan, F. Schaefer, R. Destefanis, M. Lambert. “A Ballistic Limit Equation for Hypervelocity Impacts on Composite Honeycomb Sandwich Panels Satellite Structures.” Adv. Space Res., 41(7):1152–1166, 2008.
72. F. Schaefer, S. Ryan, M. Lambert, R. Putzar. “Ballistic Limit Equation for Equipment Placed Behind Satellite Structure Walls.” Hypervelocity Impact Symposium, Williamsburg, Va., September 23–27, 2007.
73. A. Bettella, A. Francesconi, D. Pavarin, C. Giacomuzzo, F. Angrilli, Application of Wavelet Transform to analyze acceleration signals generated by HVI on thin aluminum plates and all-aluminum honeycomb sandwich panels, International Journal of Impact Engineering 35 (2008) 1427–1434

74. Iliescu, L. E., Lakis, A. A. & Oulmane, A., HYPERVELOCITY IMPACT (HVI) SIGNAL ANALYSIS, European Journal of Engineering and Technology, Vol. 4 No. 1, 2016, ISSN 2056-5860
75. M. A. Hamstad, "Comparison of Wavelet transform and Choi-Williams distribution to determine group velocities for different acoustic emission sensors"
76. Howard A. Gaberson, "Application of Choi-Williams reduced Interference time frequency distribution to machinery diagnostics"
77. L. E. Iliescu, A. A. Lakis, A. Abou – Antoun "Hypervelocity Impact (HVI) Tests & Signal Recordings", Universal Journal of Aeronautical & Aerospace Sciences 2 (2014), 80-113.
78. Mahvash, A., Lakis A.A., 2014, "Independent Component Analysis as Applied to Vibration Source Separation and Fault Diagnosis", Journal of vibration and control, online: August 2014, DQI: 10.117/107756314544349
79. A. Oulmane, A.A. Lakis and N. Mureithi. 2013, A Method for Analyzing Rotating Machinery Faults using Time-Frequency Application. International Journal of Condition Monitoring and Diagnostic Engineering Management Volume 16 No2, April 2013 pages 21-34.

ANNEX

The following tables (51) present the various mechanical properties (at room temperature, usually dependent on the environmental temperature) for:

- metal alloys

| Material | Density ρ (kg/m ³) | σ_{ν} (MPa) | σ_{ψ} (MPa) | E (GPa) |
|------------------|--|-------------------------|--------------------------|--------------|
| Aluminium | | | | |
| 2014-T6 | 2.80 | 441 | 386 | 72 |
| 2024-T36 | 2.77 | 482 | 413 | 72 |
| 6061-T6 | 2.71 | 289 | 241 | 67 |
| 7075-T6 | 2.80 | 523 | 448 | 71 |
| Magnesium | | | | |
| AZ31B | 1.77 | 221 | 110 | 44 |
| AZ31B-H24 | 1.77 | 269 | 199 | 44 |
| Titanium | | | | |
| Ti6Al-4V | 4.43 | 1103 | 999 | 110 |
| Steel | | | | |
| RH1050 | 7.60 | 1310 | 1170 | 200 |
| D6AC | 7.80 | 1600 | 1200 | 200 |
| AMS-6434 | 7.88 | 2100 | 1400 | 200 |
| Beryllium | | | | |
| Lockalloy | 2.10 | 426 | 310 | 203 |

- composite fibers

| Material | Young's modulus E (GPa) | Ultimate strength σ (MPa) | Density ρ kg/m ³ |
|-----------------------|-------------------------|----------------------------------|----------------------------------|
| E-Glass fiber* | 72.3 | 3170 | 2550 |
| S-Glass fibre* | 82.7 | 4130 | 2500 |
| E-Glass in epoxy | 51.7 | 1380 | 1940 |
| S-Glass in epoxy | 51.7 | 2070 | 1940 |
| Aramid fibre* | 137.8 | 3445 | 1690 |
| Aramid fibre in epoxy | 82.7 | 1930 | 1400 |
| HM graphite fibre* | 379 | 2070 | 1900 |
| HT graphite fibre* | 241 | 2410 | 1770 |
| AS or T-300 fibre* | 207 | 2760 | 1850 |
| HM graphite in epoxy | 207 | 930 | 1610 |
| HT graphite in epoxy | 152 | 1410 | 1500 |
| AS or T-300 in epoxy | 117 | 1580 | 1550 |
| Boron filaments* | 143 | 2760 | 2630 |
| Boron in epoxy | 214 | 1520 | 2080 |

- Al-alloy 5056 honeycomb cores

| Type of Honeycomb core | d_c | ρ | Compr. strength E_c | Shear modulus | | Shear strength | |
|------------------------|-------|----------------------|-----------------------|---------------|-------|----------------|----------|
| | (mm) | (kg/m ³) | (MPa) | (MPa) | (MPa) | (MPa) | (MPa) |
| 1/4-5056-.002p | 6.4 | 69 | 3.21 | G_L | G_T | τ_L | τ_T |
| 3/8-5056-.0007p | 9.6 | 16 | 0.24 | 462 | 186 | 2.24 | 1.31 |
| 1/4-5056-.0015p | 6.4 | 54 | 2.17 | 103 | 62 | 0.31 | 0.17 |
| 1/4-5056-.0007p | 6.4 | 26 | 0.55 | 345 | 152 | 1.59 | 0.90 |
| 3/16-5056-.002p | 4.8 | 91 | 5.07 | 138 | 83 | 0.54 | 0.26 |
| | | | | 648 | 248 | 3.31 | 1.93 |